Asian Journal of Chemistry; *Vol. 38, No. 2 (2026), 371-393*

ASIAN JOURNAL OF CHEMISTRY

https://doi.org/10.14233/ajchem.2026.35015

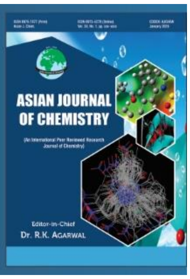

Electronic and Molecular Insights into Vericiguat: A Combined DFT, SAR and Molecular Docking Approach

D. JEBIXSON IMMANUEL and J. WINFRED JEBARAJ*

Department of Chemistry, St. John's College (Affiliated to Manonmaniam Sundaranar University, Abishekapatti), Palayamkottai, Tirunelveli-627002, India

*Corresponding author: E-mail: winfred.chem@stjohnscollege.edu.in

Received: 5 October 2025 *Accepted*: 27 December 2025 *Published online*: 31 January 2026 AJC-22255

A medication called vericiguat is employed to treat symptomatic chronic heart failure. This work utilised Gaussian 16W in the gaseous phase to perform density functional theory (DFT) algorithms at the B3LYP/6-311++G(d,p) level. The electronic structure, Mulliken charge distribution and electrostatic potential (ESP) map were analyzed to explain the fundamental properties of molecule. The hole-electron interaction studies revealed the nature of charge transfer. Theoretical vibrational and UV-Vis spectral analyses were performed to support structural characterisation. Fukui function analysis was employed to predict reactive sites toward electrophilic, nucleophilic and radical attacks. Aromaticity indices, non-covalent interaction (NCI) analysis, shaded surface mapping and localised orbital locator (LOL) projections were generated using Multiwfn 3.8. Furthermore, molecular docking and structure-activity relationship (SAR) studies were performed with Maestro (Schrödinger) against target protein 6JT2, providing insights into binding interactions and the potential therapeutic significance of vericiguat.

Keywords: Vericiguat, DFT, Electrostatic potential, Wavefunction, Hole-electron interaction, Molecular docking.

INTRODUCTION

Vericiguat is a drug that lowers the risk of heart failure-related hospitalizations and deaths from cardiovascular disease in people, who have recently had an episode of acute decompensated heart failure. This disorder, known as heart failure with reduced ejection fraction (HFrEF), is brought on by ineffective contraction of the left ventricle. The U.S. FDA granted approval for vericiguat based on results from a clinical trial involving 5,050 patients aged 23 to 98 years, all of whom had worsening heart failure. The study was carried out across 694 sites in 42 countries spanning Europe, Asia and both North and South America [1]. The nitric oxide (NO) donors have demonstrated clinical benefit in heart failure treatment, but their use is hindered by the development of tolerance over the period of time and that leads to reduced sensitivity of soluble guanylate cyclase (sGC) to nitric oxide due to reactive oxygen species [2-6]. Unlike nitric oxide donors, soluble guanylate cyclase stimulators enhance sGC activity independently of nitric oxide and simultaneously increase its sensitivity to endogenous nitric oxide [7,8]. The NO-sGC-cyclic guanosine monophosphate (*c*GMP) signaling cascade is vital in cardiovascular regulation, but this pathway becomes impaired in heart failure, leading to diminished cardio protective effects.

Given the disruption of the NO-sGC-*c*GMP signaling pathway in heart failure, the incorporation of vericiguat into treatment regimens may be considered for selected individuals with heart failure with reduced ejection fraction (HFrEF), particularly those with significantly impaired left ventricular function and an elevated risk of recurrent hospitalisations [7]. Clinical data suggest that vericiguat exhibits its most pronounced benefits in patients whose ejection fraction is below 40%. However, it appears to offer limited therapeutic effect in those classified under heart failure with preserved ejection fraction (HFpEF), typically defined by an ejection fraction ranging from 40% to 50%. This observation raises the need for further investigation into pharmacological potential of vericiguat and supports efforts toward the development of next-generation sGC modulators. Such agents would ideally offer efficacy earlier in the disease continuum, potentially slowing or halting the progression of heart failure before ventricular function declines below the critical 40% threshold, thereby improving overall survival outcomes [9].

The advancement of computational methodologies has significantly enhanced the ability to predict drug-like properties and uncover chemical dependencies. In this study, density functional theory (DFT) is employed as a computational tool to investigate vericiguat, as DFT methods are known to provide more accurate and reliable results compared to semi-empirical approaches [10]. Structurally, vericiguat consists of three six-membered rings and one five-membered ring. Among them, one pyrimidine ring contains an electron-donating substituent, while a methylcarbamate group is positioned *para*- to it. Moreover, the molecule features a pyridine ring bearing an electron withdrawing group linked to a pyrazole moiety and a terminal benzene ring substituted with fluorine. Due to the structural intricacies and electronic variations across these moieties, a comprehensive computational analysis is warranted. To validate the reliability of the structural parameters, we compared the results internally and also against structurally related compounds studied in previous researches. In particular, Shukla *et al.* [11] investigated the molecular geometry of 3-phenyl-1-(methyl sulfonyl)-1*H*-pyrazolo[3,4-*d*]pyrimidine-4-amine, a compound that shares significant structural similarity with vericiguat. The comparison of bond lengths and bond angles between the two molecules revealed a good agreement, supporting the accuracy of the computational approach [11].

Furthermore, studies by Zhang *et al*. [12] and Byru *et al*. [13] presented density functional theory (DFT) investigations on the synthesis and electronic structures of imidazo-pyrimidines and imidazo-pyrazines heterocyclic systems analogous to those found in vericiguat. Their reported structural data and electronic properties align well with the results obtained in the present study, further validating the present findings. Therefore, properties such as electronic configuration, natural bond orbital (NBO) analysis, electrostatic potential (ESP) mapping, frontier molecular orbital energy gap, Mulliken charge distribution and simulated spectral characteristics are examined to achieve a detailed understanding of the molecule. Notably, such an in-depth computational investigation of vericiguat has not been previously reported in the literature. This study thus aims to fill that gap by applying DFT-based structural and electronic analyses to this clinically significant drug.

EXPERIMENTAL

The normal 6-311++G(d,p) basis set in the gaseous phase was employed in the quantum computational operations for testing by DFT implementing Becke's three-parameter hybrid function (B3) in conjunction with the Lee-Yang-Parr (LYP) correlation level using the Gaussian 16W software program [14]. A molecular visualisation software Gaussview 06 [15,16] was used to view the characteristics and the Gausssum tool [17] confirms the convergence. For the optimal structure, theoretical calculations have been performed for the structural parameters that involve bond length, bond angle and dihedral angles. The natural bond orbital analysis, Mulliken population analysis and molecular electrostatic potential of target molecule were all computed using the same hypothetical level. The HOMO and LUMO values have been exploited to figure out chemical hardness, optical softness, chemical potential, net electrophilicity, nucleophilicity index, electrophilicity index, along with other quantum chemical parameters. The software Multiwfn 3.8 [18] was used to determine electron excitation studies, surface projection maps and other features. For displaying the iso-surfaces of the molecules acquired from the Multiwfn 3.8 tool, deploy VMD 1.9.4 software [19].

Later designed number of different vericiguat molecules were optimised are further considered for molecular docking studies using Schrodinger package. The ligand-binding domain of human soluble guanylate cyclase in the NO activated state is obtained from the protein data bank (PDB ID: 6JT2) [20,21]. Protein preparation was done using wizard of Schrödinger module for molecular docking [22]. Using Glide's receptor grid generation module, a grid was generated with a maximal size of 20 Å × 20 Å × 20 Å and 0.5 Å spacing. Docking score were calculated for the designed molecule using Maestro of Schrödinger software [23].

RESULTS AND DISCUSSION

Geometry analysis: The molecular structure of vericiguat was subjected to full geometry optimisation to obtain a stable and energetically favourable conformation using the basis set B3LYP/6-311++G(d,p). The optimisation process was carried out until convergence was achieved, as confirmed by using the GaussSum 3.0 tool. Gaussian 16W vibrational frequency analysis was implemented to guarantee sure the optimised structure reflects an authentic energy minimum on the potential energy surface. The absence of imaginary frequencies in the vibrational spectrum indicates that the optimised geometry is not a transition state but a true ground-state structure. The final optimised molecule comprises of 47 atoms and contains a total of 220 electrons. Based on the electronic configuration, vericiguat is identified as a neutral molecule in its singlet ground state.

Table-1 illustrates the list of atoms in the energy-minimised structure of the vericiguat molecule. Fig. 1 additionally shows the completely optimised and converged 2D and 3D topologies generated *via* GaussSum 3.0 software. The bond lengths, bond angles and dihedral angles of the optimised structure of vericiguat are summarised in Table-2. Since this specific molecule has not been previously characterised in detail through quantum chemical methods, there is limited literature available for direct comparison.

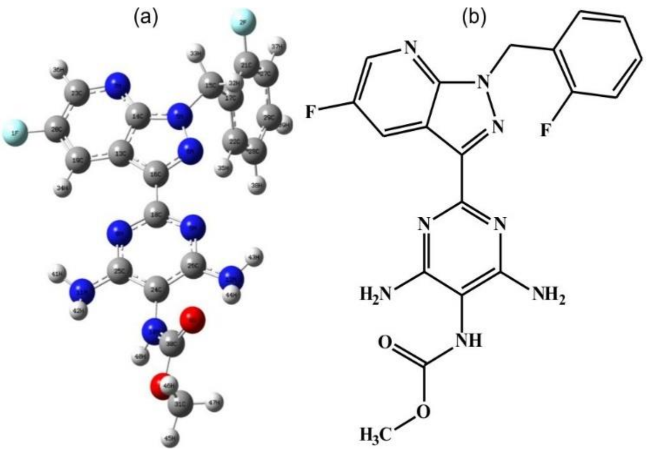

Fig. 1. (a) 3D and (b) 2D representation of vericiguat

TABLE-1
LIST OF ATOMS OF OPTIMIZED VERICIGUAT MOLECULE

1	2	3	4	5	6	7	8	9	10
C	C	N	C	C	C	N	N	C	C
11	12	13	14	15	16	17	18	19	20
C	N	C	C	N	C	N	N	N	C
21	22	23	24	25	26	27	28	29	30
C	C	C	C	C	C	F	F	O	O
31	32	33	34	35	36	37	38	39	40
C	H	H	H	H	H	H	H	H	H
41	42	43	44	45	46	47			
H	H	H	H	H	H	H			

TABLE-2
ELECTRONIC STRUCTURE VALUES OF OPTIMIZED VERICIGUAT MOLECULE

Bond length		Bond angle		Dihedral angle	
Atom set	Distance (Å)	Atom set	Angle (º)	Atom set	Angle (º)
(1C–2C)	1.419	(2C–1C–3N)	126.4	(3N–1C–2C–4C)	–0.3
(1C–3N)	1.346	(2C–1C–7N)	106.9	(3N–1C–2C–9C)	179.4
(1C–7N)	1.376	(3N–1C–7N)	126.8	(7N–1C–2C–4C)	–179.5
(2C–4C)	1.404	(1C–2C–4C)	117.6	(7N–1C–2C–9C)	0.2
(2C–9C)	1.434	(1C–2C–9C)	105.0	(2C–1C–3N–5C)	0.4
(3N–5C)	1.344	(4C–2C–9C)	137.4	(7N–1C–3N–5C)	179.5
(4C–6C)	1.380	(1C–3N–5C)	115.2	(2C–1C–7N–8N)	0.0
(4C–32H)	1.077	(2C–4C–6C)	115.6	(2C–1C–7N–10C)	–179.5
(5C–6C)	1.405	(2C–4C–32H)	121.7	(3N–1C–7N–8N)	–179.2
(5C–33H)	1.079	(6C–4C–32H)	122.7	(3N–1C–7N–10C)	1.2
(6C–28F)	1.402	(3N–5C–6C)	121.9	(1C–2C–4C–6C)	0.0
(7N–8N)	1.376	(3N–5C–33H)	117.7	(1C–2C–4C–32H)	179.8
(7N–10C)	1.459	(6C–5C–33H)	120.4	(9C–2C–4C–6C)	–179.6
(8N–9C)	1.347	(4C–6C–5C)	123.3	(9C–2C–4C–32H)	0.3
(9C–11C)	1.461	(4C–6C–28F)	119.3	(1C–2C–9C–8N)	–0.3
(10C–21C)	1.519	(5C–6C–28F)	117.4	(1C–2C–9C–11C)	179.3
(10C–34H)	1.087	(1C–7N–8N)	110.9	(4C–2C–9C–8N)	179.3
(10C–35H)	1.091	(1C–7N–10C)	127.8	(4C–2C–9C–11C)	–1.1
(11C–12N)	1.350	(8N–7N–10C)	121.3	(1C–3N–5C–6C)	–0.1
(11C–15N)	1.348	(7N–8N–9C)	107.1	(1C–3N–5C–33H)	180.0
(12N–13C)	1.364	(2C–9C–8N)	110.1	(2C–4C–6C–5C)	0.3
(13C–14C)	1.412	(2C–9C–11C)	128.2	(2C–4C–6C–28F)	–180.0
(13C–17N)	1.362	(8N–9C–11C)	121.7	(32H–4C–6C–5C)	–179.6
(14C–16C)	1.408	(7N–10C–21C)	114.0	(32H–4C–6C–28F)	0.2
(14C–19N)	1.428	(7N–10C–34H)	106.5	(3N–5C–6C–4C)	–0.2
(15N–16C)	1.355	(7N–10C–35H)	107.4	(3N–5C–6C–28F)	–180.0
(16C–18N)	1.371	(21C–10C–34H)	110.0	(33H–5C–6C–4C)	179.7
(17N–36H)	1.005	(21C–10C–35H)	110.4	(33H–5C–6C–28F)	–0.1
(17N–37H)	1.011	(34H–10C–35H)	108.3	(1C–7N–8N–9C)	–0.2
(18N–38H)	1.004	(9C–11C–12N)	116.3	(10C–7N–8N–9C)	179.4
(18–39H)	1.005	(9C–11C–15N)	118.5	(1C–7N–10C–21C)	104.8
(19N–20C)	1.362	(12N–11C–15N)	125.2	(1C–7N–10C–34H)	–16.7
(19N–40H)	1.011	(11C–12N–13C)	118.2	(1C–7N–10C–35H)	–132.6
(20C–29O)	1.245	(12N–13C–14C)	120.3	(8N–7N–10C–21C)	–74.6
(20C–30O)	1.381	(12N–13C–17N)	116.6	(8N–7N–10C–34H)	163.9
(21C–22C)	1.404	(14C–13C–17N)	123.1	(8N–7N–10C–35H)	48.0
(21C–23C)	1.392	(13C–14C–16C)	117.0	(7N–8N–9C–2C)	0.3
(22C–24C)	1.397	(13C–14C–19N)	125.0	(7N–8N–9C–11C)	–179.3
(22C–41H)	1.081	(16C–14C–19N)	117.8	(2C–9C–11C–12N)	2.2
(23C–25C)	1.386	(11C–15N–16C)	117.0	(2C–9C–11C–15N)	–178.5
(23C–27F)	1.408	(14C–16C–15N)	122.1	(8N–9C–11C–12C)	–178.3
(24C–26C)	1.399	(14C–16C–18N)	121.6	(8N–9C–11C–15N)	1.1
(24C–42H)	1.081	(15N–16C–18N)	116.2	(7N–10C–21C–22C)	46.1
(25C–26C)	1.396	(13C–17N–36H)	116.2	(7N–10C–21C–23C)	–135.7
(25C–43H)	1.080	(13C–17N–37H)	119.5	(34H–10C–21C–22C)	165.7

(26C–44H)	1.081	(36H–17N–37H)	119.0	(34H–10C–21C–23C)	–16.2
(29O–37H)	1.959	(16C–18N–38H)	121.3	(35H–10C–21C–22C)	–74.8
(30O–31C)	1.469	(16C–18N–39H)	116.5	(35H–10C–21C–23C)	103.3
(31C–45H)	1.084	(38H–18N–39H)	119.0	(9C–11C–12N–13C)	–177.4
(31C–46H)	1.087	(14C–19N–20C)	127.7	(15N–11C–12N–13)	3.3
		(14C–19N–40H)	116.9	(9C–11C–15N–16C)	177.6
		(20C–19N–40H)	115.3	(12N–11C–15N–16C)	–3.2
		(19N–20C–29O)	126.6	(11C–12N–13C–14C)	0.8
		(19N–20C–30O)	109.8	(11C–12N–13C–17N)	–179.7
		(29O–20–30O)	123.6	(12N–13C–14C–16C)	–4.4
		(10C–21C–22C)	122.6	(12N–13C–14C–19N)	169.5
		(10C–21C–23C)	120.5	(17N–13C–14C–16C)	176.1
		(22C–21C–23C)	116.9	(17N–13C–14C–19N)	–10.0
		(21C–22C–24C)	120.8	(12N–13N–17N–36H)	0.1
		(21C–22C–41H)	118.6	(12N–13C–17N–37H)	154.0
		(24C–22C–41H)	120.6	(14C–13C–17N–36H)	179.6
		(21C–23C–25C)	123.8	(14C–13C–17N–37H)	–26.5
		(21C–23C–27F)	118.5	(13C–14C–16C–15N)	4.6
		(25C–23C–27F)	117.7	(13C–14C–16C–18N)	–177.9
		(22C–24C–26C)	120.4	(19N–14C–16C–15N)	–169.8
		(22C–24C–42H)	119.6	(19N–14C–16C–18N)	7.7
		(26C–24C–42H)	120.0	(13C–14C–19N–20C)	49.3
		(23C–25C–26C)	118.3	(13C–14C–19N–40H)	–127.6
		(23C–25C–43H)	119.6	(16C–14C–19C–20C)	–136.8
		(26C–25C–43H)	122.1	(16C–14C–19N–40H)	46.3
		(24C–26C–25C)	119.8	(11C–15N–16C–14C)	–1.0
		(24C–26C–44H)	120.4	(11C–15N–16C–18N)	–178.6
		(25C–26C–44H)	119.7	(14C–16C–18N–38H)	20.8
		(20C–30O–31C)	116.5	(14C–16C–18N–39H)	–179.8
		(30O–31C–45H)	104.6	(15N–16C–18N–38H)	–161.6
		(30O–31C–46H)	110.2	(15N–16C–18N–39H)	–2.2
		(30O–31C–47H)	110.2	(14C–19N–20C–29O)	–3.7
		(45H–31C–46H)	111.2	(14C–19N–20–30O)	177.2
		(45H–31C–47H)	110.9	(40H–19N–20C–29O)	173.2
		(46H–31C–47H)	109.6	(40H–19N–20C–30O)	–5.9
				(19N–20C–30O–31C)	177.6
				(29O–20C–30O–31C)	–1.5
				(10C–21C–22C–24C)	178.9
				(10C–21C–22C–41H)	–1.5
				(23C–21C–22C–24C)	0.7
				(23C–21C–22C–41H)	–179.7
				(10C–21C–23C–25C)	–178.9
				(10C–21C–23C–27F)	0.8
				(22C–21C–23C–25C)	–0.7
				(22C–21C–23C–27F)	179.0
				(21C–22C–24C–26C)	–0.3
				(21C–22C–24C–42H)	179.8
				(41H–22C–24C–26C)	–180.0
				(41H–22C–24C–42H)	0.2
				(21C–23C–25C–26C)	0.3
				(21C–23C–25C–43H)	–179.7
				(27F–23C–25C–26C)	–179.4
				(27F–23C–25C–43H)	0.6
				(22C–24C–26C–25C)	–0.1
				(22C–24C–26C–44H)	180.0
				(42H–24C–26C–25C)	179.8
				(42H–24C–26C–44H)	–0.1
				(23C–25C–26C–24C)	0.1
				(23C–25C–26C–44H)	–180.0
				(43H–25C–26C–24C)	–179.9
				(43H–25C–26C–44H)	0.0
				(20C–30O–31C–45H)	177.2
				(20C–30O–31C–46H)	57.6
				(20C–30O–31C–47H)	–63.5

TABLE-3
MULLIKAN CHARGE FOR EACH ATOM OF VERICIGUAT MOLECULE

Atom	Charge (a.u.)	Atom	Charge (a.u.)	Atom	Charge (a.u.)	Atom	Charge (a.u.)
1C	0.5568	13C	0.6016	25C	-0.1838	37H	0.3535
2C	-0.3926	14C	0.1416	26C	-0.1168	38H	0.3252
3N	-0.3190	15N	-0.3791	27F	-0.3395	39H	0.3390
4C	0.0880	16C	0.5254	28F	-0.3380	40H	0.3516
5C	-0.0065	17N	-0.8158	29O	-0.4489	41H	0.1991
6C	0.1955	18N	-0.8261	30O	-0.5020	42H	0.1554
7N	-0.5520	19N	-0.7837	31C	-0.2683	43H	0.1775
8N	-0.1989	20C	0.6873	32H	0.2120	44H	0.1584
9C	0.1728	21C	-0.0469	33H	0.1996	45H	0.1983
10C	-0.2469	22C	-0.0737	34H	0.2410	46H	0.2047
11C	0.3140	23C	0.2818	35H	0.2268	47H	0.1992
12N	-0.4344	24C	-0.1594	36H	0.3262		

Among the calculated bond lengths, the shortest C–H bond is observed at the 4C–32H position, measuring 1.077 Å and the longest C–H bond is found at two positions at equal distance on 10C–34H and 31C–46H of around 1.087 Å. Overall, the longest bond length 1.959 Å, is recorded at the 29O–37H position and the shortest is recorded at two positions 17N–36H and 18N–39H with the same distance of about 1.005Å. The largest and shortest bond angles of vericiguat are about 137.4º and 104.6º, respectively. The bond angles are also consistent with expected values; for example, the calculated C–C–C bond angle is found to be 120.4º, closely matching the experimentally reported value of 120.0º [24]. Similarly, the computed C–C–N bond angle is 110.1º, which is in excellent agreement with the experimental value of 110.0º [25]. These results confirm the reliability and accuracy of the optimised geometry obtained through DFT calculations.

Mullikan charge analysis: The Mulliken atomic charges of the target molecule were calculated using the same level of theory and basis set and the results are presented in Table-3. The charge distribution can be seen visually in Fig. 2 as well. Given that the two oxygen atoms designated 29O and 30O have different Mulliken charge values of –0.4489 a.u. and –0.5020 a.u., respectively, it is clear from Table-3 and Fig. 2 that these molecules are not composed of the same electrical properties. This variation suggests distinct electronic environments and potentially different roles in chemical reactivity or molecular interactions.

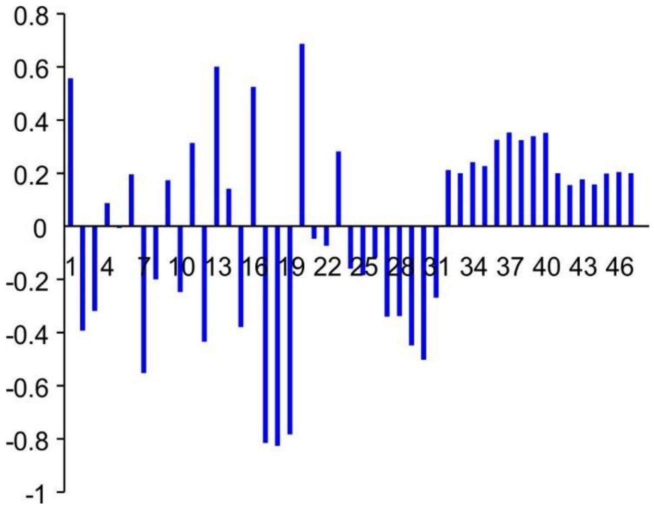

Fig. 2. Mulliken charge diagram of vericiguat molecule

Furthermore, the carbon atom designated as 20C exhibits the highest positive charge among all atoms, with a value of +0.6873 a.u., highlighting its electron-deficient nature. In contrast, the nitrogen atom labeled as 18N carries the most negative charge in the molecule, at –0.8261 a.u., suggesting a significant accumulation of electron density in its vicinity. These charge extremes may correspond to key reactive sites and can be strategically targeted for specialised chemical modifications or biological interactions. As expected, all hydrogen atoms in the molecule exhibit positive Mulliken charges, in line with their typical electropositive character. This observation is confirmed by the computed charge values and aligns with the general trend seen in similar molecular systems.

Quantum chemical parameter: DFT using B3LYP/6-311++G(d,p) level of theory was used to derive the chemical reactivity parameters using HOMO and LUMO values [26] (Table-4). Fig. 3 displays the HOMO and LUMO of the entire molecule.

TABLE-4
CALCULATED QUANTUM CHEMICAL PARAMETERS OF VERICIGUAT MOLECULE

S. No.	Physical parameters	Charge (eV)
1	HOMO	-1.7464
2	LUMO	-5.9520
3	Energy gap (ΔE)	4.2061
4	Ionization potential (I)	1.7464
5	Electron affinity (A)	5.9520
6	Electro negativity (χ)	3.8495
7	Chemical potential (μ)	-3.8495
8	Chemical hardness (η)	-2.1030
9	Chemical softness	-0.4755
10	Electrophilicity index (ω)	-3.5232
11	Electron accepting capacity (ω^+)	-5.7107
12	Electron donating capacity (ω^-)	-1.8612
13	Net electrophilicity ($\Delta\omega^\pm$)	-3.8495
14	Global softness (S)	-0.2378
15	Electron back donation	0.5258
16	Nucleophilicity index	-0.2838
17	Additional electronic charge	-1.8305
18	Optical softness	0.2377

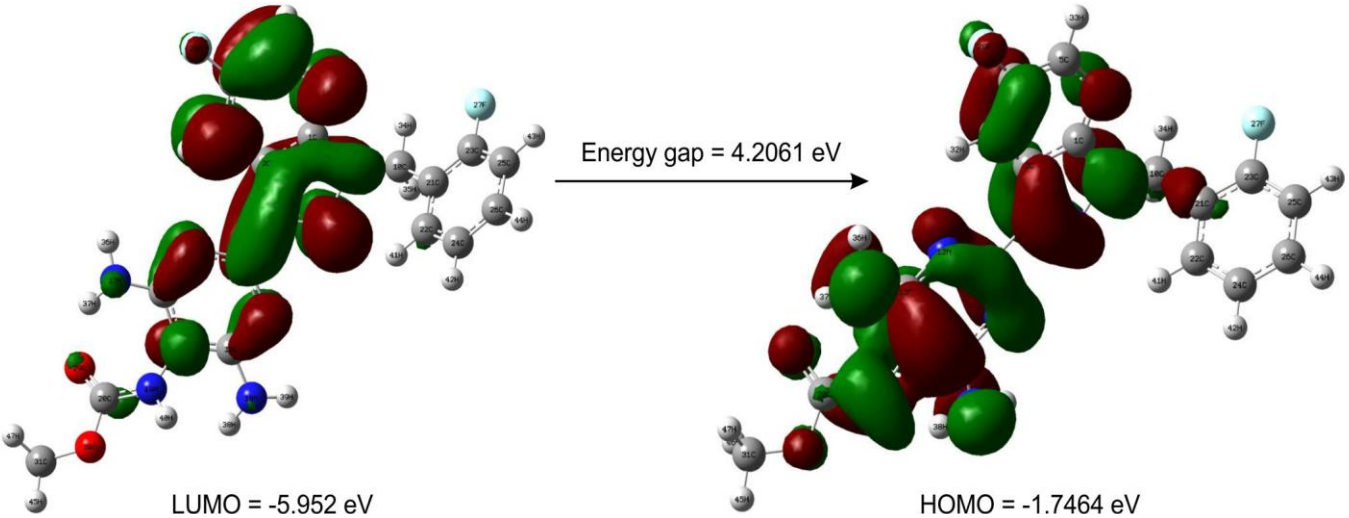

Fig. 3. HOMO-LUMO of vericiguat molecule

Ionisation potential and electron affinity: The capacity of chemical species to take and give one electron can be assessed by electron affinity (A) and ionisation potential (I) (eqns. 1 and 2). They are defined as:

$$A = -E_{LUMO} \quad (1)$$

$$I = -E_{HOMO} \quad (2)$$

where E_{HOMO} and E_{LUMO} are the energies of highest occupied and lowest unoccupied molecular orbitals, respectively.

Electronegativity (χ) and chemical potential (μ): Electronegativity (χ) (eqn. 3) is a frequently utilized chemical characteristic that denotes the tendency of an atom or group to attract electrons and can be represented using eqn. 3 [27,28]. It is the inverse of the chemical potential (μ).

$$\chi = \frac{I + A}{2} \quad (3)$$

The energy of the lowest unoccupied molecular orbital (LUMO) and the highest occupied molecular orbital (HOMO) can be utilized to modify the electron affinity and ionization potential, respectively (eqn. 4), according to Koopman's theorem [29]:

$$\chi = -\mu = -\frac{E_{HOMO} + E_{LUMO}}{2} \quad (4)$$

Global hardness and softness: Eqn. 5 demonstrates that the energy difference between occupied and unoccupied molecular orbitals corresponds to global hardness (η). Global softness (S), an additional molecular property, has a relationship with it (eqn. 6) and it is the reciprocal of hardness [28].

$$\eta = \frac{E_{HOMO} - E_{LUMO}}{2} \quad (5)$$

$$S = \frac{1}{\eta} \quad (6)$$

Electrophilicity and net electrophilicity: Electrophilicity is the ability of an electrophile to acquire electrons from the nucleophile (eqn. 7). Both chemical potential and hardness have been used for assessing the electrophilicity in DFT [30, 31].

$$\omega = \frac{\mu^2}{2\eta} \quad (7)$$

Using electron-accepting (ω^+) and electron-donating (ω^-) powers, net electrophilicity ($\Delta\omega^{\pm}$) (eqn. 8) have been proposed [32].

$$\Delta\omega^{\pm} = \omega^+ - (\omega^-) \quad (8)$$

$$\omega^- = \frac{(3I + A)}{2} \quad (9)$$

$$\omega^+ = \frac{(I + 3A)}{16(I - A)} \quad (10)$$

Higher the value of ω^+ corresponds the molecule's ability to attract electrons and greater capacity for charge acceptance and a smaller ω^- values improves the electron-donating capacity [33]. A biological activity is also influenced by the nucleophilicity and electrophilicity parameters. As the nucleophilicity index increases, the reactivity of the molecule increases [34].

The HOMO-LUMO values indicate that verciguat is more inclined to absorb electrons than to donate them, while the moderate energy gap indicates that vericiguat possesses an equitable balance of chemical reactivity and kinetic stability, rendering it appropriate for biological activity. Global softness reflects good polarizability, suitable for soft biological interactions. Additional electronic charge transfer (–1.8305 eV), negative value implies that vericiguat may resist further electron accumulation, again reflecting electrophilic predominance. The optical softness (positive) and global softness value (negative) also indicates good response to electronic excitation, which is crucial for photochemical or UV-visible properties.

Electrostatic potential map (MEP): The electrostatic potential map of the title molecule was computed using the B3LYP/6-311++G(d,p) method. The resulting MEP surface, highlighting various electrostatic regions, is shown in Fig. 4a. A notable red region indicating high electron density is observed between the two nitrogen atoms located in adjacent rings, suggesting a potential site for electrophilic attack. Widespread blue regions appear near hydrogen atoms bonded to more

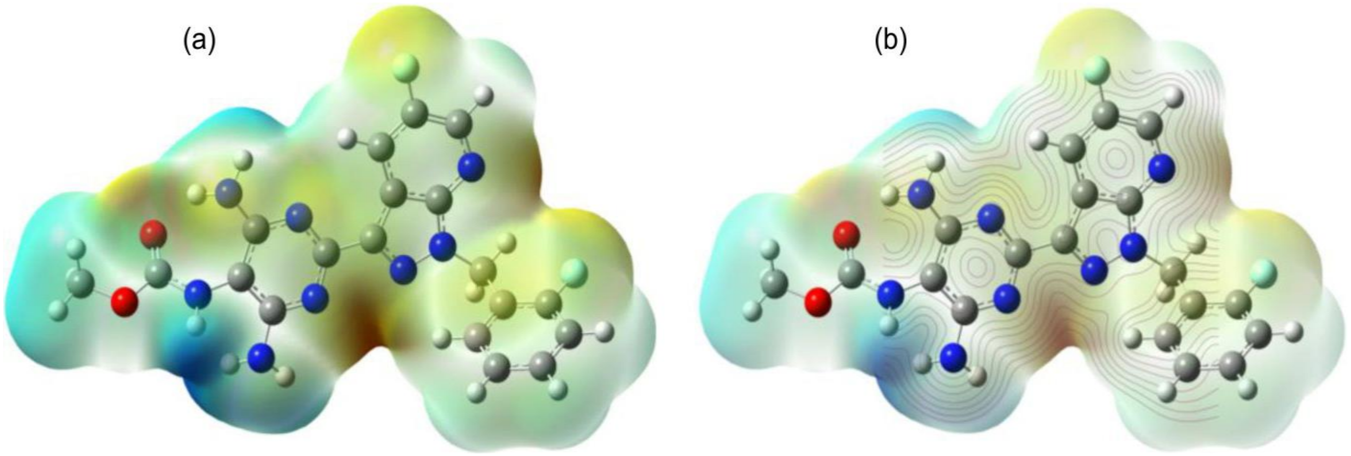

Fig. 4. (a) MEP and (b) Contour diagrams of vericiguat molecule

electronegative atoms, making these sites favourable for nucleophilic attack. Furthermore, the contour map of the molecule (Fig. 4b) provides further spatial insight into the charge distribution. From this map, the key regions for potential chemical reactivity and further active site analysis can be clearly identified.

Natural bond orbital analysis: Analysis of the natural bond orbital (NBO) takes place out at the theoretical level B3LYP/6-311++G(d,p). Eqn. 11, utilized to ascertain the stabilization energy E(2), is associated with donor-acceptor orbital overlap, derived from second-order perturbation theory [35,36]. The key donor-acceptor NBO interactions are summarized and illustrated in Fig. 5.

$$E(2) = \frac{q_i F(i,j)^2}{\varepsilon_j - \varepsilon_i} \tag{11}$$

From the NBO analysis, electron delocalisation and charge transfer pathways across the system can be clearly visualised. In the studied molecule, three rings were considered, allow to trace the electron flow from ring 1 to ring 3 and the charge values are shown in Table-5. Notably, ring 3 contains a fluorine substituent, which acts as a strong electron-withdrawing group, making it the focal point for analyzing electron redistribution. In ring 1, the presence of one NH group and two -NH_2 groups facilitates electron transfer in different directions. Specifically, from N19–H40, electron transfer is slightly higher towards side A (1.66 kcal/mol) compared to side B (1.41 kcal/mol). From N18–H38–H39, electron flow is also higher towards side A (0.68 kcal/mol) than side B (0.57 kcal/mol). Conversely, from N17–H36–H37, electron transfer is more prominent towards side B (4.39 kcal/mol) compared to side A (0.72

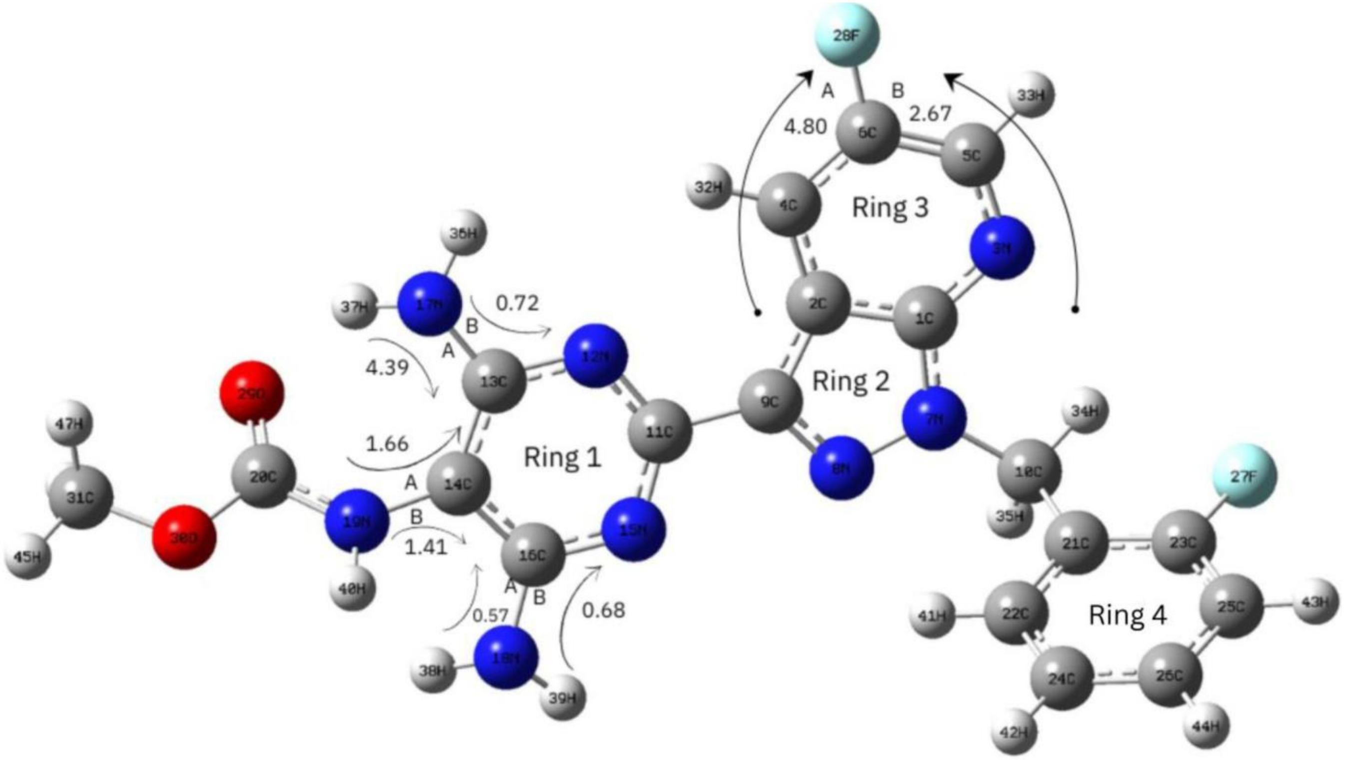

Fig. 5. Natural bond orbital (NBO) analysis pictorial representation of vericiguat molecule

TABLE-5
NATURAL BOND ORBITAL (NBO) VALUES OF VERICIGUAT MOLECULE

Type	Donor NBO (i)	ED/e (a.u.)	Type	Acceptor NBO (j)	ED/e (a.u.)	E(2) (kcal/mol)	E(j)-E(i) (a.u.)	F(i,j) (a.u.)
σ	C1–C2	1.96365	σ*	N7–C10	0.03010	5.51	0.99	0.066
σ	C1–C2	1.96365	σ*	C9–C11	0.04140	4.59	1.15	0.065
σ	C2–C4	1.96770	σ*	C1–C2	0.03606	3.42	1.23	0.058
σ	C2–C4	1.96770	σ*	C4–C6	0.02351	2.32	1.28	0.049
σ	C2–C4	1.96770	σ*	C6–F 28	0.03468	4.80	0.92	0.059
σ	C2–C9	1.96959	σ*	C1–N3	0.02082	5.15	1.19	0.070
σ	C2–C9	1.96959	σ*	C2–C4	0.02006	4.78	1.23	0.069
σ	N3–C5	1.97934	σ*	C1–N7	0.05359	5.55	1.27	0.076
σ	N3–C5	1.97934	σ*	C6–F 28	0.03468	2.67	1.04	0.047
π	N3–C5	1.78009	LP*(1)	C1	0.97852	49.38	0.18	0.107
π	N3–C5	1.78009	π*	C4–C6	0.30777	12.21	0.33	0.058
π	C4–C6	1.69482	LP (1)	C2	1.05620	38.15	0.16	0.089
π	C4–C6	1.69482	π*	N3–C5	0.37495	26.21	0.27	0.076
π	N7–C10	1.58217	LP*(1)	C1	0.97852	99.42	0.15	0.128
π	N7–C10	1.58217	π*	N8–C9	0.38086	29.02	0.28	0.081
π	N7–C10	1.58217	σ*	C10–C21	0.02879	5.53	0.79	0.066
π	N8–C9	1.84164	LP (1)	C2	1.05620	24.27	0.19	0.082
π	N8–C9	1.84164	π*	C11–N15	0.43751	12.53	0.31	0.060
σ	C9–C11	1.96988	σ*	C2–C9	0.03114	2.78	1.18	0.051
σ	C10–C21	1.78598	π*	N7–C10	0.49974	157.29	1.15	0.411
σ	C10–C21	1.78598	σ*	C10–C21	0.02879	7.97	1.00	0.084
σ	C10–C21	1.78598	σ*	C10–H 35	0.01871	16.04	0.98	0.118
σ	C10–H 34	1.92356	σ*	N7–N8	0.02313	5.39	0.82	0.060
σ	C10–H 34	1.92356	π*	N7–C10	0.49974	45.46	1.14	0.229
σ	C10–H 34	1.92356	σ*	C10–C21	0.02879	5.77	0.99	0.068
σ	C10–H 34	1.92356	σ*	C10–H 35	0.01871	8.04	0.96	0.080
σ	C10–H 35	1.68460	π*	N7–C10	0.49974	314.99	0.95	0.512
σ	C10–H 35	1.68460	σ*	C10–C21	0.02879	38.93	0.79	0.169
σ	C10–H 35	1.68460	σ*	C10–H 34	0.01193	9.19	0.70	0.078
σ	C10–H 35	1.68460	σ*	C10–H 35	0.01871	17.73	0.77	0.113
σ	C11–N12	1.98211	σ*	C13–N17	0.02513	3.27	1.29	0.058
σ	C11–N15	1.98103	σ*	C16–N18	0.02764	3.79	1.27	0.062
π	C11–N15	1.74559	π*	N8–C9	0.38086	9.53	0.30	0.049
π	C11–N15	1.74559	π*	N12–C13	0.50753	6.34	0.29	0.041
π	C11–N15	1.74559	π*	C14–C16	0.43874	32.03	0.30	0.092
σ	N12–C13	1.97946	σ*	C14–N19	0.02624	3.11	1.19	0.054
π	N12–C13	1.68998	π*	C11–N15	0.43751	39.34	0.30	0.100
π	N12–C13	1.68998	π*	C14–C16	0.43874	7.31	0.30	0.043
σ	C13–C14	1.97216	σ*	C14–C16	0.03819	3.55	1.25	0.060
σ	C13–C14	1.97216	σ*	C16–N18	0.02764	3.49	1.17	0.057
σ	C14–C16	1.97194	σ*	C13–C14	0.03924	3.35	1.25	0.058
σ	C14–C16	1.97194	σ*	C13–N17	0.02513	3.57	1.19	0.058
π	C14–C16	1.65975	π*	C11–N15	0.43751	8.45	0.28	0.044
π	C14–C16	1.65975	π*	N12–C13	0.50753	34.91	0.26	0.089
σ	N15–C16	1.97943	σ*	C9–C11	0.04140	3.16	1.28	0.057
σ	N17–H 36	1.98829	σ*	C13–C14	0.03924	4.39	1.18	0.065
σ	N17–H 37	1.98341	σ*	N12–C13	0.02130	3.80	1.15	0.059
π	C21–C23	1.66471	π*	C22–C24	0.31734	19.01	0.31	0.069
π	C21–C23	1.66471	π*	C25–C26	0.34107	18.28	0.31	0.067
π	C22–C24	1.66372	π*	C21–C23	0.38359	19.74	0.27	0.066
π	C22–C24	1.66372	π*	C25–C26	0.34107	21.06	0.29	0.070
π	C25–C26	1.67900	π*	C21–C23	0.38359	22.39	0.28	0.072
π	C25–C26	1.67900	π*	C22–C24	0.31734	17.67	0.30	0.065
σ	O30–C31	1.99040	σ*	C23–F 27	0.03682	10.95	0.97	0.092
σ	O30–C31	1.99040	σ*	C24–C26	0.01542	12.70	1.31	0.115
σ	O30–C31	1.99040	σ*	C25–H 43	0.01232	8.60	1.19	0.090
σ	O30–C31	1.99040	σ*	C31–H 45	0.00759	6.94	2.98	0.128
σ	O30–C31	1.99040	σ*	C31–H 46	0.01187	18.34	4.74	0.263

σ	O30–C31	1.99040	σ*	C31–H 47	0.01226	20.61	3.91	0.254
σ	C31–H 45	1.99243	π*	C22–C24	0.31734	5.36	0.59	0.055
σ	C31–H 45	1.99243	σ*	C23–F 27	0.03682	12.28	0.71	0.084
σ	C31–H 45	1.99243	σ*	C24–C26	0.01542	13.02	1.04	0.104
σ	C31–H 45	1.99243	σ*	C25–H 43	0.01232	8.56	0.93	0.080
σ	C31–H 45	1.99243	σ*	C31–H 46	0.01187	26.52	4.48	0.308
σ	C31–H 45	1.99243	σ*	C31–H 47	0.01226	14.00	3.65	0.202
σ	C31–H 46	1.99580	σ*	C23–F 27	0.03682	11.99	0.70	0.083
σ	C31–H 46	1.99580	σ*	C24–C26	0.01542	12.68	1.04	0.103
σ	C31–H 46	1.99580	σ*	C25–H 43	0.01232	8.45	0.93	0.079
σ	C31–H 46	1.99580	σ*	C31–H 46	0.01187	12.52	4.47	0.212
σ	C31–H 46	1.99580	σ*	C31–H 47	0.01226	42.31	3.65	0.351
σ	C31–H 47	1.99561	σ*	N7–C10	0.03010	7.22	0.77	0.067
σ	C31–H 47	1.99561	π*	N7–C10	0.49974	5.47	1.13	0.081
σ	C31–H 47	1.99561	π*	C22–C24	0.31734	10.16	0.50	0.069
σ	C31–H 47	1.99561	σ*	C23–F 27	0.03682	35.70	0.62	0.134
σ	C31–H 47	1.99561	σ*	C24–C26	0.01542	36.19	0.96	0.167
σ	C31–H 47	1.99561	π*	C25–C26	0.34107	6.11	0.50	0.054
σ	C31–H 47	1.99561	σ*	C25–H 43	0.01232	24.51	0.85	0.129
σ	C31–H 47	1.99561	σ*	C31–H 46	0.01187	50.38	4.39	0.421
σ	C31–H 47	1.99561	σ*	C31–H 47	0.01226	66.39	3.56	0.435
π*	N3–C5	0.37495	π*	C4–C6	0.30777	119.48	0.02	0.083
π*	N12–C13	0.50753	π*	C11–N15	0.43751	274.07	0.01	0.076
π*	N12–C13	0.50753	π*	C14–C16	0.43874	281.53	0.01	0.079
π*	C21–C23	0.38359	π*	C22–C24	0.31734	172.15	0.02	0.083
π*	C21–C23	0.38359	π*	C25–C26	0.34107	184.82	0.02	0.082
σ	N19–H 40	1.97723	σ*	C13–C14	0.03924	1.66	1.21	0.040
σ	N18–H 38	1.98784	π*	C14–C16	0.43874	0.57	0.69	0.020
σ	N18–H 38	1.98784	σ*	N15–C16	0.01870	3.67	1.19	0.059
σ	N18–H 39	1.98958	σ*	C14–C16	0.03819	3.99	1.20	0.062
σ	N18–H 39	1.98958	σ*	N15–C16	0.01870	0.68	1.18	0.025
σ	N7–N8	1.98402	σ*	C1–N3	0.02082	3.60	1.34	0.062
σ	N7–N8	1.98402	σ*	C9–C11	0.04140	3.43	1.30	0.060
σ	C1–N7	1.98623	σ*	C1–N3	0.02082	1.57	1.33	0.041
σ	C1–N3	1.98313	σ*	N3–C5	0.00910	0.80	1.36	0.029
σ	C5–C6	1.98653	σ*	C4–C6	0.02351	3.37	1.30	0.059
σ	C6–F 28	1.99479	σ*	C2–C4	0.02006	1.25	1.49	0.039
σ	C6–F 28	1.99479	σ*	N3–C5	0.00910	1.45	1.47	0.041

E(2) means energy of hyperconjugative interactions (stabilisation energy). eD/e means the electron density. Energy difference between donor and acceptor i and j NBO orbitals. F(i, j) is the Fock matrix element between i and j NBO orbital. LP(n)A is a valence lone pair orbital (n) on A atom.

kcal/mol). Furthermore, the electron flow from ring 1 propagates efficiently towards ring 3 containing fluorine, following two distinct pathways. Between these, path A (C2-C4) (4.80 kcal/mol) is energetically more favourable than path B (2.67 kcal/mol), indicating a stronger preference for electron delocalisation along path A towards the fluorine substituent.

Hole-electron interaction: Vericiguat molecule contains two amino groups (electron donors) connected through π-linkers, along with two strong electron-withdrawing fluorine substituents, one attached to the pyridine ring and the other to the benzene ring. Since fluorine and amino groups are electron acceptors and donors during electron excitation, respectively, it is anticipated that vericiguat should display charge-transfer (CT) states involving electron displacement from the amino groups toward the fluorine substituent present at the pyridine moiety. This prompted an investigation into the electron excitation properties of this chemical.

The IOP (9/40 = 4) term was utilized to obtain the optimized geometry of vericiguat at the B3LYP/6-311++G(d,p) theoretical level and only investigated the fifteen lowest singlet excited states. Table-6 summarizes the parameters under investigation at the theoretical level, including Sm, Sr, D, H, τ indices, excitation energy, Coulomb attraction energy, Δr and Λ (Lambda) values. In addition, the hole-electron distribution, C_{hole}-C_{elec} function, Sr function and charge density difference (CDD) were also calculated and shown in Fig. 6.

The analysis revealed that the highest D index values occur for the S0→S12 and S0→S14 transitions, indicating clear CT excitations. This conclusion is also supported by the centroid separation between the blue (hole) and green (electron) isosurfaces in Fig. 6, where the $C_{hole} – C_{elec}$ centers are significantly displaced for these states. In addition, the S0→S1, S3, S4, S5, S11 and S13 transitions exhibit moderately elevated D indices, suggesting that CT excitations may also play a role in these states.

Most excited states exhibit comparatively elevated Sr index values, except for S0→S12 and S0→S14, which may alternatively adhere to n→π* transitions localized on the benzene, nitro or acetyl groups. For standard n→π* transitions, Sr values are anticipated to approximate 0.8 a.u. [37]; however, this

TABLE-6
HOLE-ELECTRON INTERACTION PARAMETERS OF VERICIGUAT MOLECULE

Excitation states	Sm (a.u.)	Sr (a.u.)	D index (Å)	H index (Å)	τ index (Å)	Excitation energy (eV)	Coloumb attractive energy (eV)	Δr (Å)	Λ
S1	0.379	0.660	1.379	3.176	-0.936	4.307	3.914	0.667	2.653
S2	0.240	0.521	0.957	2.789	-1.084	4.560	4.492	0.610	1.314
S3	0.413	0.669	1.544	3.100	-0.861	4.824	3.844	0.619	1.996
S4	0.237	0.472	1.164	2.186	-0.232	4.905	5.363	0.455	2.483
S5	0.397	0.663	1.584	3.333	-0.794	4.994	3.453	0.598	2.029
S6	0.535	0.777	0.692	3.227	-1.570	5.215	4.040	0.631	1.320
S7	0.552	0.755	0.150	3.580	-1.694	5.524	2.998	0.662	0.793
S8	0.450	0.699	0.868	3.974	-2.072	5.533	2.972	0.661	1.433
S9	0.243	0.466	0.902	3.096	-0.769	5.613	2.965	0.538	2.396
S10	0.277	0.500	0.844	3.096	-0.782	5.660	3.010	0.552	2.164
S11	0.325	0.597	2.235	3.099	0.033	5.834	3.150	0.571	1.912
S12	0.049	0.187	4.993	2.561	3.365	5.952	2.288	0.188	5.145
S13	0.300	0.566	1.566	3.573	-1.093	6.062	2.755	0.601	1.270
S14	0.036	0.151	5.178	3.573	3.486	6.115	2.409	0.210	5.021
S15	0.203	0.420	0.969	2.715	-1.145	6.176	3.739	0.502	2.572

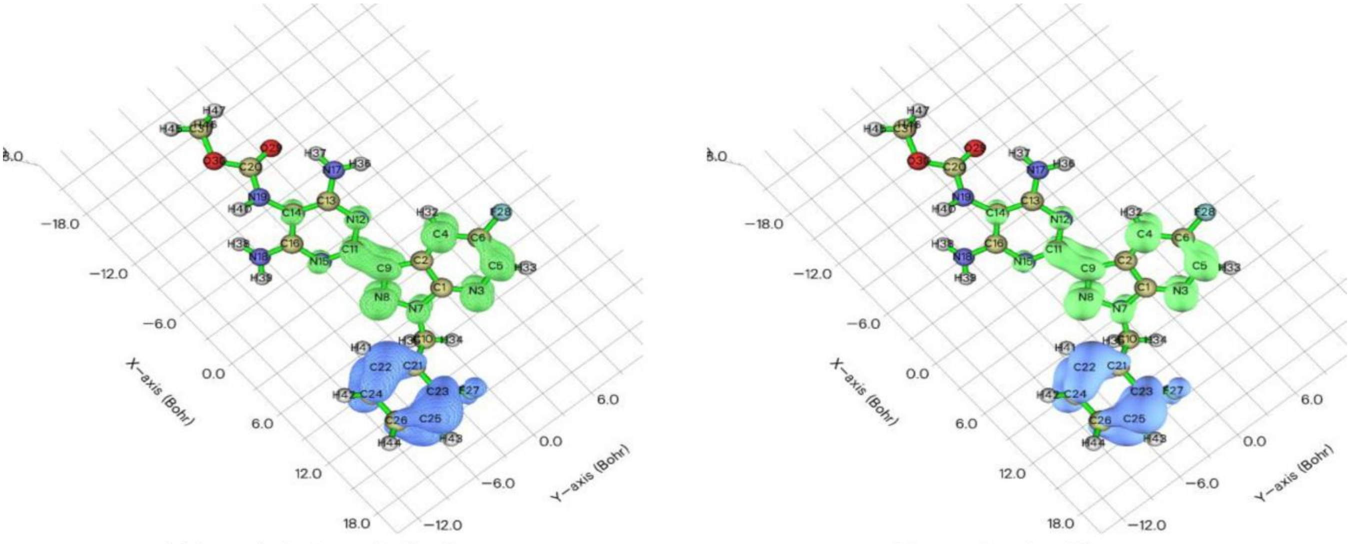

Hole and electron distribution

Charge density difference

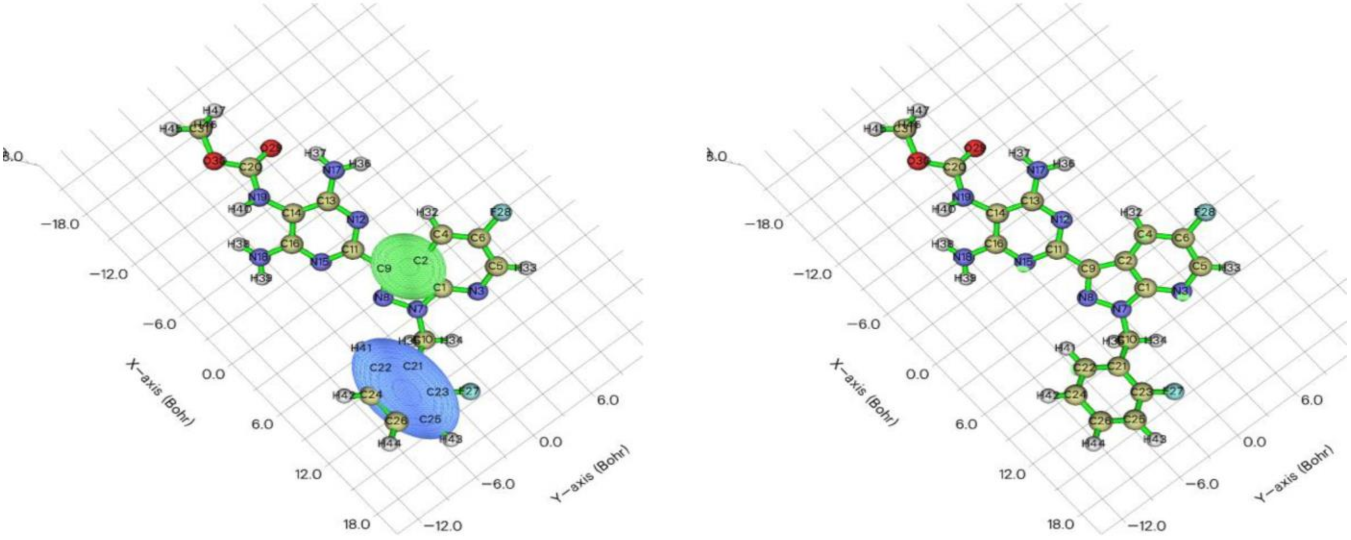

C_{hole}–C_{elec} function

Overlap of hole-electron Sr function

Fig. 6. Hole electron interaction of excited state: 14 (S0→S14)

behaviour is not manifested, signifying the non-existence of $\pi\rightarrow\pi^*$ transitions in these excitations. The τ index validates these observations. Positive τ values for S0→S11, S12 and S14 indicate substantial hole-electron separation, indicative of charge transfer (CT) excitations. Conversely, negative τ values for the remaining excited states indicate negligible spatial separation, aligning with local excitation (LE) characteristics.

The Coulomb attraction energy values (Table-6) offer insights into excitation behaviour. The D index is a critical determinant; a bigger D index signifies enhanced hole-electron separation and as a result, diminished Coulombic attraction. The S0→S14 state demonstrates the second lowest Coulomb attraction energy (2.409 eV) among all excitations, aligning with its elevated D index. The Δr and Λ values further validate the CT characteristics of S0→S12 and S0→S14. The states have low Δr values (0.188 and 0.210, respectively), indicating a pronounced CT character, whereas the elevated Δr values of the other states imply LE character. In contrast, Λ values exhibit an inverse trend: bigger Λ values for S0→S12 and S0→S14 signify more robust CT excitations, while smaller values for the other states suggest local excitations.

Vibrational analysis: The interaction between infrared (IR) radiation and matter provides key insights into molecular structure, functional groups and characteristic bonding patterns. The target drug molecule contains 47 atoms arranged across multiple planes, leading to 295 fundamental vibrational modes. Of these, 157 correspond to in-plane vibrations (A′ symmetry), while 138 are out-of-plane vibrations (A″ symmetry). The complete vibrational spectrum was computed using the DFT/B3LYP/6-311++G(d,p) basis set and the simulated IR spectrum is shown in Fig. 7 and the IR values are summarised in Table-7.

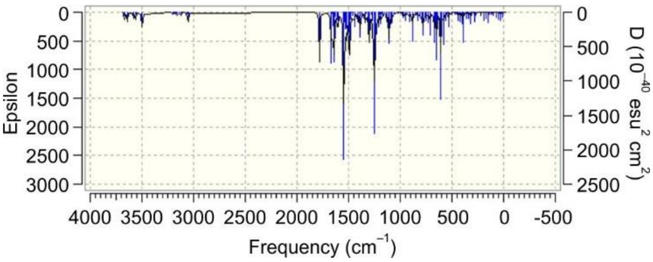

Fig. 7. Theoretical IR spectrum of vericiguat

The calculated vibrational spectrum exhibits specific characteristics attributable to the stretching, bending, scissoring, torsional and wagging movements of diverse functional groups. In the high-frequency region, characteristic N–H vibrations are clearly observed. The symmetric stretching of the NH_2 group is calculated at 3380 and 3442 cm^{-1}, while the asymmetric stretching appears at slightly higher frequencies of 3522 and 3548 cm^{-1}. Similarly, the NH stretching vibration of the amine group is identified at 3459 cm^{-1}. C–H stretching vibrations are well defined, with CH_2 symmetric stretching at 2960 cm^{-1} and CH_3 symmetric stretching at 2949 cm^{-1}. The CH stretching bands of the pyrazolo-pyridine framework are also prominent, appearing in the range 3129-3064 cm^{-1}, which is consistent with the reported C–H stretching of this heteroaromatic scaffold.

The mid-frequency region of the spectrum is dominated by carbonyl, carbon–nitrogen and carbon–carbon stretching vibrations. The C=O stretching band appears strongly at 1722 cm^{-1}, confirming the presence of the carbonyl functionality. The CC stretching vibrations are widely distributed across 1601-818 cm^{-1}, reflecting both aromatic and aliphatic contributions. The NC stretching bands are particularly intense and

TABLE-7
THEORETICAL IR VALUES OF VERICIGUAT

Mode. No	Symmetry	Frequency	Scaled (0.9668)	Intensity	Assignment with PED
1	A′	3670	3548	vw	τ_{as} $N^{18}H^{38}$ (51), τ_{as} $N^{18}H^{39}$ (49)
2	A′	3643	3522	w	τ_{as} $N^{17}H^{36}$ (83), τ_{as} $N^{17}H^{37}$ (17)
3	A′	3577	3459	vw	τ $N^{19}H^{40}$ (100)
4	A′	3560	3442	vw	τ_s $N^{18}H^{38}$ (49), τ_s $N^{18}H^{39}$ (50)
5	A′	3496	3380	m	τ_s $N^{17}H^{36}$ (17), τ_s $N^{17}H^{37}$ (83)
6	A′	3236	3129	vw	τ $C^{4}H^{32}$ (100)
7	A′	3202	3095	vw	τ $C^{25}H^{43}$ (71), τ $C^{26}H^{44}$ (18)
8	A′	3194	3088	vw	τ $C^{22}H^{41}$ (48), τ $C^{24}H^{42}$ (33), τ $C^{25}H^{43}$ (16)
9	A′	3184	3079	vw	τ $C^{22}H^{41}$ (39), τ $C^{24}H^{42}$ (16), τ $C^{26}H^{44}$ (36)
10	A′	3172	3067	vw	τ $C^{24}H^{42}$ (44), τ $C^{26}H^{44}$ (43)
11	A′	3170	3064	vw	τ $C^{5}H^{33}$ (100)
12	A′	3157	3052	vw	τ_{as} $C^{31}H^{45}$ (81), τ_{as} $C^{31}H^{46}$ (11)
13	A′	3141	3037	vw	τ_{as} $C^{10}H^{34}$ (90), τ_{as} $C^{10}H^{35}$ (10)
14	A′	3123	3019	vw	τ_{as} $C^{31}H^{46}$ (51), τ_{as} $C^{31}H^{47}$ (49)
15	A′	3062	2960	vw	τ_s $C^{10}H^{34}$ (10), τ_s $C^{10}H^{35}$ (90)
16	A′	3050	2949	vw	τ_s $C^{31}H^{45}$ (19), τ_s $C^{31}H^{46}$ (38), τ_s $C^{31}H^{47}$ (43)
17	A′	1781	1722	m	τ $C^{20}O^{29}$ (75)
18	A′	1665	1610	s	τ_s $N^{17}C^{13}$ (10), ω $H^{37}N^{17}H^{36}$ (58)
19	A′	1656	1601	vw	τ $C^{23}C^{25}$ (13), τ $C^{21}C^{23}$ (12), τ $C^{22}C^{24}$ (29)
20	A′	1647	1592	w	τ_s $N^{3}C^{1}$ (17), τ $C^{2}C^{4}$ (26), ω $H^{39}N^{18}H^{38}$ (14)
21	A′	1643	1589	m	ω $H^{39}N^{18}H^{38}$ (48)
22	A′	1627	1573	vw	τ $C^{21}C^{23}$ (18), τ $C^{26}C^{25}$ (31), δ $C^{22}C^{24}C^{26}$ (12)

23	A′	1611	1558	vw	τ N^{3}C^{1} (11), τ_{s} C^{6}C^{5} (20)
24	A′	1609	1555	vw	τ N^{12}C^{13} (19), τ C^{14}C^{16} (12)
25	A′	1601	1548	w	τ N^{15}C^{11} (16), τ C^{14}C^{16} (13)
26	A′	1546	1495	vs	τ N^{19}C^{20} (20), η H^{40}N^{19}C^{20} (45)
27	A′	1535	1484	vw	τ C^{4}C^{6} (22), τ C^{11}C^{9} (18)
28	A′	1525	1474	w	τ C^{21}C^{23} (12), η H^{41}C^{22}C^{24} (18), η H^{43}C^{25}C^{26} (15)
29	A′	1522	1471	w	τ N^{8}C^{9} (14)
30	A′	1502	1452	w	ω H^{47}C^{31}H^{46} (68), β H^{47}C^{31}O^{30}C^{20} (10)
31	A′	1494	1444	m	τ N^{17}C^{13} (17)
32	A′	1488	1439	w	η H^{42}C^{24}C^{26} (24), η H^{44}C^{26}C^{25} (23)
33	A′	1483	1434	vw	ω H^{45}C^{31}H^{47} (40), ω H^{46}C^{31}H^{45} (33), β H^{45}C^{31}O^{30}C^{20} (18)
34	A′	1477	1428	vw	ω H^{35}C^{10}H^{34} (45)
35	A′	1471	1422	vw	μ H^{45}C^{31}H^{47} (26), μ H^{46}C^{31}H^{45} (34)
36	A′	1460	1412	vw	τ N^{8}C^{9} (10), τ N^{7}C^{1} (10), ω H^{35}C^{10}H^{34} (14)
37	A′	1444	1396	w	τ N^{7}C^{1} (14)
38	A′	1414	1367	vw	τ N^{3}C^{5} (11), τ N^{8}C^{9} (17), τ N^{12}C^{11} (13)
39	A′	1411	1365	vw	τ N^{8}C^{9} (13), η H^{34}C^{10} C^{21} (22), β H^{34}C^{10}C^{21}C^{22} (14)
40	A′	1387	1341	w	τ N^{3}C^{5} (13), δ H^{33}C^{5}N^{3} (22), β H^{35}C^{10}C^{21}C^{22} (12)
41	A′	1368	1323	vw	τ_{s} N^{3}C^{5} (22)
42	A′	1339	1294	vw	δ C^{2}C^{4}C^{6} (17), δ C^{9}N^{8}N^{7} (10)
43	A′	1335	1291	vw	τ_{s} N^{12}C^{11} (20), τ_{s} N^{15}C^{16} (18), τ_{s} N^{12}C^{13} (15)
44	A′	1331	1287	vw	τ_{s} C^{23}C^{25} (18), τ_{s} C^{22}C^{24} (16), τ_{s} C^{24}C^{26} (14)
45	A′	1312	1269	w	δ H^{41}C^{22}C^{24} (27), δ H^{43}C^{25}C^{26} (11)
46	A′	1300	1256	w	τ_{s} N^{8}N^{7} (12), β H^{35}C^{10}C^{21}C^{22} (12)
47	A′	1282	1239	vw	τ_{s} N^{19}C^{14} (29), δ H^{36}N^{17}C^{13} (16), δ H^{40}N^{19}C^{20} (10)
48	A′	1267	1225	vw	τ_{s} N^{3}C^{5} (14), δ H^{32}C^{4}C^{6} (10), δ H^{33}C^{5}N^{3} (33)
49	A′	1254	1212	s	τ_{s} N^{19}C^{20} (18), τ_{s} O^{30}C^{20} (26), δ H^{40}N^{19}C^{20} (13), δ O^{29} C^{20}O^{30} (11)
50	A′	1252	1210	w	τ_{s} C^{23}C^{25} (11), τ_{s} C^{26}C^{25} (15), τ_{s} F^{27}C^{23} (32)
51	A′	1236	1195	m	τ_{s} F^{28}C^{6} (16)
52	A′	1213	1172	w	μ H^{47}C^{31}H^{46} (18), β H^{46}C^{31}O^{30}C^{20} (29), β H^{47}C^{31}O^{30}C^{20} (30)
53	A′	1203	1163	vw	τ_{s} C^{10}C^{21} (16), δ H^{42}C^{24}C^{26} (14)
54	A′	1186	1147	w	τ_{s} N^{8}N^{7} (14), δ H^{32}C^{4}C^{6} (10), δ H^{34}C^{10}C^{21} (10), δ H^{42}C^{22}C^{26} (12)
55	A′	1177	1138	vw	μ H^{45}C^{31}H^{47} (12), μ H^{46}C^{31}H^{45} (10), β H^{45}C^{31}O^{30}C^{20} (28), β H^{46}C^{31}O^{30}C^{20} (11), β H^{47}C^{31}O^{30}C^{20} (15)
56	A′	1175	1136	vw	τ_{s} C^{14}C^{16} (13), δ H^{38}N^{18}C^{16} (12), β H^{45}C^{31}O^{30}C^{20}(10)
57	A′	1174	1135	vw	δ H^{43}C^{25}C^{26} (23), δ H^{44}C^{26}C^{25} (30)
58	A′	1130	1092	vw	δ H^{32}C^{4}C^{6} (14)
59	A′	1111	1074	vw	τ_{s} N^{8}N^{7} (12)
60	A′	1108	1071	w	τ_{s} N^{12}C^{13} (13), τ_{s} O^{30}C^{31} (11), δ H^{36}N^{17}C^{13} (18)
61	A′	1091	1055	vw	τ_{s} N^{12}C^{13} (10), τ_{s} O^{30}C^{31} (15), δ H^{38}N^{18}C^{16} (12)
62	A′	1077	1041	vw	τ_{s} N^{15}C^{16} (14), τ_{s} O^{30}C^{31} (22)
63	A′	1057	1022	vw	τ_{s} C^{22}C^{24} (12), τ_{s} C^{26}C^{25} (17), τ_{s} C^{24}C^{26} (36)
64	A′	1024	990	vw	δ C^{2}C^{4} C^{6} (11), δ H^{32}C^{4}C^{6} (10)
65	A″	1005	972	vw	β H^{41}C^{22}C^{24}C^{26} (41), β H^{42}C^{24}C^{26}C^{25} (33)
66	A″	979	946	vw	β H^{44}C^{26}C^{25}C^{23} (18)
67	A″	973	941	vw	β H^{44}C^{26}C^{25}C^{23} (17)
68	A′	969	936	vw	τ_{s} O^{30}C^{20} (14), τ_{s} O^{30}C^{31} (16), δ O^{30}C^{20}N^{19} (10)
69	A′	952	921	vw	δ H^{34}C^{10} C^{21} (10), β H^{34}C^{10}C^{21}C^{22} (11)
70	A″	934	903	vw	β H^{32}C^{4}C^{6}C^{5} (39), β H^{33}C^{5}N^{3}C^{1} (54)
71	A″	913	883	vw	β H^{32}C^{4}C^{6}C^{5} (40), β H^{33}C^{5}N^{3}C^{1} (32), γ F^{28}C^{4}C^{5}C^{6} (14)
72	A′	884	854	w	δ N^{12}C^{11}N^{15} (16)
73	A″	879	850	vw	β H^{41}C^{22}C^{24}C^{26} (16), β H^{42}C^{24}C^{26}C^{25} (20), β H^{43}C^{25}C^{26}C^{24} (43)
74	A′	846	818	vw	τ_{s} F^{28}C^{6} (18), τ_{s} C^{10}C^{21} (13), δ C^{22}C^{24}C^{26} (18)
75	A″	826	799	vw	β C^{14}C^{16}N^{15}C^{11} (18), γ N^{18}C^{14}N^{15}C^{16} (10), γ N^{12}C^{9}N^{15}C^{11} (26)
76	A′	806	780	vw	δ N^{7}C^{10}C^{21} (11)
77	A″	805	778	vw	β C^{6}C^{5}N^{3}C^{1} (15)
78	A′	793	767	vw	δ C^{4}C^{6}C^{5} (10)
79	A″	792	766	vw	β C^{6}C^{5}N^{3}C^{1} (11)
80	A″	779	753	vw	γ O^{29}N^{19}O^{30}C^{20} (83)

81	A″	776	750	w	$\beta\ H^{41}C^{22}C^{24}C^{26}$ (10), $\beta\ H^{42}C^{24}C^{26}C^{25}$ (31), $\beta\ H^{44}C^{26}C^{25}C^{23}$ (33), $\gamma\ F^{27}C^{21}C^{25}C^{23}$ (12)
82	A′	761	735	vw	$\gamma\ N^{12}C^{9}N^{15}C^{11}$ (12)
83	A″	751	726	vw	$\gamma\ N^{12}C^{9}N^{15}C^{11}$ (16)
84	A′	734	710	vw	$\delta\ O^{29}C^{20}O^{30}$ (28), $\gamma\ N^{17}C^{14}N^{12}C^{13}$ (13)
85	A′	714	690	w	$\delta\ O^{29}C^{20}O^{30}$ (12), $\beta\ H^{37}N^{17}C^{13}C^{14}$ (10), $\gamma\ N^{18}C^{14}N^{15}C^{16}$ (26), $\gamma\ N^{17}C^{14}N^{12}C^{13}$ (13)
86	A″	708	684	vw	$\beta\ C^{21}C^{23}C^{25}C^{26}$ (17), $\beta\ C^{22}C^{24}C^{26}C^{25}$ (15), $\beta\ C^{24}C^{26}C^{25}C^{23}$ (14)
87	A″	672	649	w	$\beta\ H^{37}N^{17}C^{13}C^{14}$ (11), $\beta\ C^{4}C^{6}C^{5}N^{3}$ (10), $\beta\ C^{6}C^{5}N^{3}C^{1}$ (10)
88	A′	657	636	vw	$\delta\ C^{6}C^{5}N^{3}$ (13)
89	A″	648	627	w	$\beta\ H^{36}N^{17}C^{13}C^{14}$ (11), $\beta\ H^{37}N^{17}C^{13}C^{14}$ (13), $\gamma\ N^{17}C^{14}N^{12}C^{13}$ (13)
90	A′	642	620	vw	$\delta\ N^{18}C^{16}N^{15}$ (10)
91	A″	614	594	vw	$\beta\ C^{4}C^{6}C^{5}N^{3}$ (12), $\gamma\ N^{8}C^{10}C^{1}N^{7}$ (14)
92	A″	610	590	m	$\beta\ H^{38}N^{18}C^{16}C^{14}$ (18), $\beta\ H^{39}N^{18}C^{16}C^{14}$ (13), $\beta\ H^{40}N^{19}C^{20}O^{30}$ (28), $\gamma\ N^{18}C^{14}N^{15}C^{16}$ (10)
93	A′	598	578	vw	$\delta\ C^{23}C^{25}C^{26}$ (18)
94	A′	596	576	vw	$\delta\ N^{12}C^{11}N^{15}$ (13), $\beta\ H^{39}N^{18}C^{16}C^{14}$ (13), $\beta\ H^{40}N^{19}C^{20}O^{30}$ (26)
95	A′	584	564	w	$\delta\ C^{13}N^{12}C^{11}$ (12), $\beta\ H^{39}N^{18}C^{16}C^{14}$ (29), $\beta\ H^{40}N^{19}C^{20}O^{30}$ (13)
96	A′	564	545	vw	$\delta\ C^{14}C^{16}N^{15}$ (12), $\delta\ C^{16}N^{15}C^{11}$ (24), $\delta\ C^{13}N^{12}C^{11}$ (12), $\beta\ H^{39}N^{18}C^{16}C^{14}$ (12)
97	A″	555	537	vw	$\beta\ C^{22}C^{24}C^{26}C^{25}$ (16)
98	A′	543	525	vw	$\delta\ N^{17}C^{13}N^{12}$ (11), $\beta\ C^{22}C^{24}C^{26}C^{25}$ (13), $\gamma\ F^{27}C^{21}C^{25}C^{23}$ (12)
99	A″	532	515	vw	$\beta\ H^{36}N^{17}C^{13}C^{14}$ (56), $\beta\ H^{37}N^{17}C^{13}C^{14}$ (24)
100	A′	525	508	vw	$\tau_s\ F^{28}C^{6}$ (10), $\delta\ C^{21}C^{23}C^{25}$ (13), $\gamma\ F^{27}C^{21}C^{25}C^{23}$ (12)
101	A′	504	487	vw	$\delta\ F^{27}C^{23}C^{25}$ (21)
102	A′	468	453	vw	$\delta\ C^{5}N^{3}C^{1}$ (16), $\delta\ F^{27}C^{23}C^{25}$ (10)
103	A″	459	444	vw	$\beta\ H^{32}C^{4}C^{6}C^{5}$ (11), $\beta\ C^{2}C^{4}C^{6}C^{5}$ (14), $\gamma\ F^{28}C^{4}C^{5}C^{6}$ (29)
104	A″	446	431	vw	$\beta\ C^{21}C^{23}C^{25}C^{26}$ (10), $\beta\ C^{24}C^{26}C^{25}C^{23}$ (25)
105	A′	441	427	vw	$\delta\ F^{27}C^{23}C^{25}$ (22)
106	A″	420	406	vw	$\beta\ C^{2}C^{4}C^{6}C^{5}$ (10), $\gamma\ N^{19}C^{13}C^{16}C^{14}$ (14)
107	A′	397	384	vw	$\delta\ F^{28}C^{6}C^{5}$ (20), $\beta\ H^{38}N^{18}C^{16}C^{14}$ (20), $\beta\ H^{40}N^{19}C^{20}O^{30}$ (10)
108	A′	393	380	vw	$\delta\ F^{28}C^{6}C^{5}$ (28), $\beta\ H^{38}N^{18}C^{16}C^{14}$ (10)
109	A″	364	352	vw	$\beta\ H^{38}N^{18}C^{16}C^{14}$ (18)
110	A′	340	328	vw	$\delta\ C^{31}O^{30}C^{20}$ (18), $\beta\ C^{5}N^{3}C^{1}N^{7}$ (11)
111	A′	321	310	vw	$\delta\ C^{31}O^{30}C^{20}$ (13), $\gamma\ N^{19}C^{13}C^{16}C^{14}$ (10)
112	A′	315	304	vw	$\delta\ N^{17}C^{13}N^{12}$ (26)
113	A″	288	278	vw	$\gamma\ F^{27}C^{21}C^{25}C^{23}$ (12), $\gamma\ C^{10}C^{22}C^{23}C^{21}$ (14)
114	A′	278	269	vw	$\delta\ N^{18}C^{16}N^{15}$ (12), $\delta\ N^{19}C^{14}C^{16}$ (29), $\delta\ C^{31}O^{30}C^{20}$ (15)
115	A′	268	259	vw	$\delta\ C^{10}C^{21}C^{23}$ (12)
116	A″	249	241	vw	$\beta\ C^{21}C^{23}C^{25}C^{26}$ (13), $\gamma\ F^{27}C^{21}C^{25}C^{23}$ (12)
117	A′	234	227	vw	$\beta\ C^{16}N^{15}C^{11}C^{9}$ (22), $\beta\ C^{13}N^{12}C^{11}C^{9}$ (27)
118	A′	224	216	vw	$\delta\ C^{10}C^{21}C^{23}$ (15)
119	A′	216	209	vw	
120	A″	195	188	vw	$\beta\ C^{5}N^{3}C^{1}N^{7}$ (12), $\beta\ N^{3}C^{1}N^{7}C^{10}$ (19), $\beta\ C^{14}C^{16}N^{15}C^{11}$ (15)
121	A′	169	163	vw	$\delta\ O^{30}C^{20}N^{19}$ (10), $\beta\ C^{31}O^{30}C^{20}N^{19}$ (11)
122	A″	160	155	vw	$\beta\ C^{21}C^{23}C^{25}C^{26}$ (13), $\beta\ C^{31}O^{30}C^{20}N^{19}$ (17)
123	A″	153	147	vw	$\beta\ C^{20}N^{19}C^{14}C^{13}$ (12), $\beta\ C^{31}O^{30}C^{20}N^{19}$ (31)
124	A′	144	139	vw	$\delta\ C^{1}N^{7}C^{10}$ (15), $\delta\ C^{10}C^{21}C^{23}$ (16)
125	A″	117	113	vw	$\gamma\ C^{10}C^{22}C^{23}C^{21}$ (17)
126	A″	110	106	vw	$\beta\ C^{5}N^{3}C^{1}N^{7}$ (13), $\beta\ N^{3}C^{1}N^{7}C^{10}$ (10), $\beta\ C^{20}N^{19}C^{14}C^{13}$ (14)
127	A″	97	94	vw	$\beta\ H^{46}C^{31}O^{30}C^{20}$ (12), $\beta\ C^{31}O^{30}C^{20}N^{19}$ (10), $\gamma\ C^{11}C^{2}N^{8}C^{9}$ (10)
128	A′	78	76	vw	$\beta\ C^{20}N^{19}C^{14}C^{13}$ (20), $\beta\ C^{31}O^{30}C^{20}N^{19}$ (25)
129	A′	73	71	vw	$\delta\ N^{15}C^{11}C^{9}$ (13), $\delta\ C^{11}C^{9}N^{8}$ (23), $\beta\ O^{30}C^{20}N^{19}C^{14}$ (37)
130	A′	51	49	vw	$\delta\ N^{15}C^{11}C^{9}$ (11), $\delta\ C^{20}N^{19}C^{14}$ (14), $\delta\ N^{19}C^{14}C^{16}$ (10), $\beta\ O^{30}C^{20}N^{19}C^{14}$ (14)
131	A′	37	36	vw	$\delta\ C^{11}C^{9}N^{8}$ (10), $\beta\ O^{30}C^{20}N^{19}C^{14}$ (13)
132	A″	26	25	vw	$\beta\ N^{15}C^{11}C^{9}C^{2}$ (26), $\beta\ C^{16}N^{15}C^{11}C^{9}$ (13), $\beta\ C^{1}N^{7}C^{10}C^{21}$ (10)
133	A″	21	20	vw	$\beta\ N^{15}C^{11}C^{9}C^{2}$ (12), $\beta\ N^{7}C^{10}C^{21}C^{22}$ (35), $\gamma\ C^{11}C^{2}N^{8}C^{9}$ (12)
134	A″	15	14	vw	$\beta\ N^{15}C^{11}C^{9}C^{2}$ (47), $\beta\ N^{7}C^{10}C^{21}C^{22}$ (12)
135	A″	9	9	vw	$\beta\ C^{1}N^{7}C^{10}C^{21}$ (60), $\beta\ N^{7}C^{10}C^{21}C^{22}$ (15)

occur over a broad range (1610-1041 cm^{-1}), consistent with the nitrogen-rich nature of the molecule. The N-N stretching modes are assigned to bands at 1256 and 1074 cm^{-1}, while CO stretching vibrations are observed at 1212, 1055, 1041 and 936 cm^{-1}. Additional features due to C–F stretching appear at 1210, 1195, 818, 508 cm^{-1}.

Bending vibrations provide further confirmation of the molecular framework. The H–C–H scissoring vibration is observed around 1452-1412 cm^{-1}, while H–N–H scissoring bands appear between 1610 and 1589 cm^{-1}. In-plane bending vibrations such as CCC, CCN and CNC occur in the lower to mid-frequency range (1573-216 cm^{-1}), whereas COC and FCC in-plane bends are assigned below 450 cm^{-1}. Out-of-plane bending vibrations are also evident, with CCC modes at 578-139 cm^{-1}, CCN and CNC vibrations below 600 cm^{-1} and HCC and HNC modes observed at 921 and 1055 cm^{-1}, respectively.

The low-frequency region is dominated by torsional and wagging motions, which are sensitive to the conformational flexibility of the molecule. Torsional modes of the backbone, including CCCC, CCCN and CCNC, appear between 799 and 155 cm^{-1}. More complex torsional interactions involving heteroatoms (CNCN, COCN, HNCC, HCOC and OCNC) span the range of 1341-9 cm^{-1}, with notable intensity around 690-384 cm^{-1}. Finally, the wagging vibrations of the H–C–H groups are observed at 1422, 1172 and 1138 cm^{-1}, completing the vibrational description of the molecule.

Comparison with experimental and literature data: The B3LYP/6-311++G(d,p) methodology yielded theoretical vibrational frequencies that are in excellent agreement with actual infrared data published for comparable heteroaromatic and nitrogen-rich medicinal compounds. For instance, the calculated C=O stretching at 1722 cm^{-1} is consistent with the typical experimental range of 1730-1700 cm^{-1} for carbonyl groups in conjugated systems [38]. Likewise, the CH stretching modes observed in the 3129-3064 cm^{-1} region closely match the experimental values reported for pyrazolo- and pyridine-based derivatives (3177-3170 cm^{-1}) [39]. The NH$_2$ stretching bands, both symmetric (3442-3380 cm^{-1}) and asymmetric (3548-3522 cm^{-1}), also correlate well with experimental amine frequencies (3550-3300 cm^{-1}) [40].

Minor deviations between the calculated and experimental frequencies are expected, primarily due to anharmonic effects and the absence of solvent and environmental interactions in the gas-phase computational model. To minimize such discrepancies, a scaling factor is often applied to the theoretical frequencies, which brings the computed spectrum into even closer alignment with experimental IR results. Thus, the comparative analysis confirms that the theoretical predictions are reliable and accurately reproduce the vibrational characteristics of the drug molecule. This close agreement validates the use of the DFT/B3LYP/6-311G++(d,p) method for the present system and provides strong evidence for the structural assignments made from the simulated IR spectrum.

Simulated UV-Visible spectrum analysis: Fig. 8 illustrates the theoretical UV-Vis spectra of the studied molecule in the 200-450 nm range for ethanol solution. Theoretical UV-Vis spectra based on the B3LYP/6-311++G(d,p) level for ethanol solvent was calculated using the DFT technique. Table-8 lists the energy (cm^{-1}), wavelength (nm), oscillator strength (f) and major and minor contributions for the molecule in ethanol solvent. The HOMO for this molecule is found at MO 110. In ethanol solvent, the title molecule exhibits three peaks. The values of the simulated spectrum occur at 349.8, 295.4 and 291.0 nm.

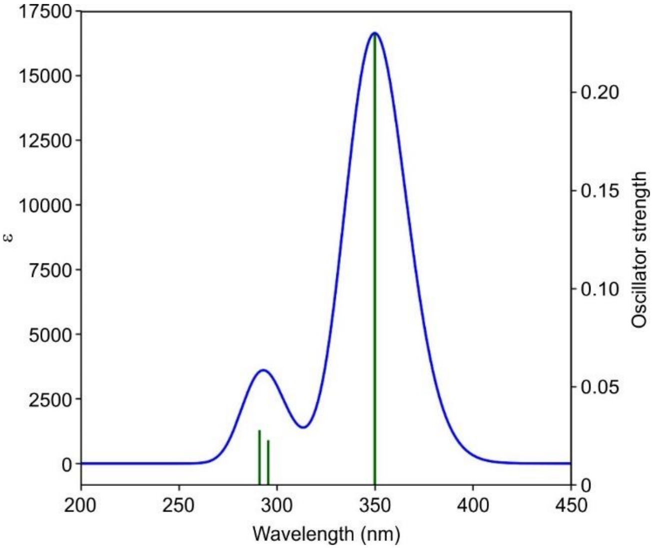

Fig. 8. UV spectrum of vericiguatin in ethanol solvent

The HOMO-LUMO (98%) contribution is responsible for the peak at 349.8 nm, corresponding to an energy of 28585.1 cm^{-1}. The peak at 295.4 nm, corresponding to an energy of 33849.5 cm^{-1}, is attributed mostly to the contributions of HOMO-2→LUMO (17%) and HOMO-1→LUMO (55%), with minor contributions from HOMO-5→LUMO (8%), HOMO-4→LUMO (8%), HOMO-4→LUMO+1 (2%) and HOMO→LUMO+1 (6%). A peak at 34363.3 cm^{-1} is observed at 291.0

TABLE-8
SIMULATED UV-VIS DATA OBTAINED FOR VERICIGUAT IN ETHANOL SOLVENT

S. No.	Energy (cm^{-1})	Calculated wavelength (nm)	Osc. strength (f)	Major contributions	Minor contributions
1	28585.1	349.8	0.2297	HOMO→LUMO (98%)	–
2	33849.5	295.4	0.0228	HOMO-2→LUMO (17%), HOMO1→LUMO (55%)	HOMO-5→LUMO (8%), HOMO4→LUMO (8%), HOMO-4→LUMO+1 (2%), HOMO→LUMO+1 (6%)
3	34363.3	291.0	0.028	HOMO-2→LUMO (57%), HOMO1→LUMO (31%)	HOMO-4→LUMO (4%), HOMO→LUMO+4 (2%)

nm, mostly due to substantial contributions from HOMO-2 →LUMO (57%) and HOMO-1→LUMO (31%), along with modest contributions from HOMO-4→LUMO (4%) and HOMO →LUMO+4 (2%). The strengths of the three oscillators are 0.028, 0.0228 and 0.2297.

Fukui Function analysis: The Fukui function quantifies the change in electron density that occurs when an electron is either added to or removed from the system [36]. Specifically, it determines which atoms are chemically vulnerable by analyzing the response of electron density at a particular atomic location to these changes. Mathematically, the Fukui function is expressed as:

$$f(k) = \frac{\partial n(k)}{\partial N} \tag{12}$$

where f(k) represents the Fukui function for a particular atom k; n(k) is the electron density at atom k; and N is the total number of electrons in molecule.

$$\Delta f(r) = [f_j^{+} - f_j^{-}] \tag{13}$$

The present study uses the Gaussian package at the B3LYP/6-311++G(d,p) level of theory to look into the optimised molecular structure at the neutral, cationic and anionic states. The corresponding results were obtained through natural population analysis (NPA) and Mulliken population analysis (MPA) and presented in Table-9. Based on these atomic charges, the Fukui function was constructed to assess local reactivity descriptors.

In both natural population analysis (NPA) and Mulliken population analysis (MPA), the Fukui function values provide insights into the type of chemical attack a given atomic site may undergo. A positive value indicates a lower electron density around the atom, suggesting susceptibility to nucleophilic attack. Conversely, a negative value signifies a higher electron density, making the site favourable for electrophilic attack and the values close to zero indicate the possibility of radical attack. These considerations are key factors in interpreting the Fukui function. For title molecule, vericiguat, Table-9 reveal that in MPA analysis, atoms 1C, 20C and 13C exhibit high positive values in the cationic, anionic and neutral states, respectively, indicating that these atoms are the most vulnerable to nucleophilic attack. Similarly, NPA results suggest that 20C, 11C and 16C show consistently higher positive values across all states. Therefore, the overall order of nucleophilic susceptibility can be summarised as 20C > 11C >1C > 16C > 13C.

In contrast, for electrophilic attack, MPA analysis shows that 19N, 18N and 17N possess strongly negative values in the cationic, anionic and neutral states, respectively, making them more prone to electrophilic attack. The NPA values also confirmed this trend, with 18N, 17N and 15N consistently exhibiting high negative values across all states. Thus, the order of electrophilic susceptibility is 18N > 17N > 15N > 12N > 29O. According to Δf dual descriptor values (2C, 13C, 16C, 31C, 19N, 21C, 22C, 7N, 41H) are having negative values and they are prone to electrophilic attack, other sites have positive values, therefore they will more possibly encounter nucleophilic attack.

Aromaticity analysis: The structure of the molecule being studied includes three aromatic rings. The aromaticity of these rings for the headline molecule was examined and contrasted with one another at the DFT/B3LYP/6-311G++(d,p) level of theory. The para delocalisation index (PDI) [41], bird aromaticity [42], aromatic fluctuation index (FLU) [43], harmonic oscillator measure of aromaticity (HOMA) [44] and PLR [45], data obtained using the Multiwfn 3.8 software are displayed in Table-10. The FLU (eqn. 14), PDI (eqn. 15), HOMA (eqn. 16), BIRD aromaticity (eqn. 17) and PLR aromaticity (eqn. 18) are defined as follows:

$$\mathrm{FLU} = \frac{1}{n}\sum_{A-B}^{\mathrm{ring}}\left[\left(\frac{V(B)}{V(A)}\right)^{\alpha}\left(\frac{\delta(A,B)-\delta_{\mathrm{ref}}(A,B)}{\delta_{\mathrm{ref}}(A,B)}\right)\right]^{2} \tag{14}$$

where n is equal to the number of atoms in ring; δ_{ref} is the reference DI value, which is pre-calculated parameter. α is used to ensure the ratio of atomic valences is greater than one.

$$\mathrm{PDI} = \frac{\delta(1,4)+\delta(2,5)+\delta(3,6)}{3} \tag{15}$$

$$\mathrm{HOMA} = 1-\sum_{i}\frac{\alpha_{i,j}}{N}(R_{\mathrm{ref}}-R_{i,j})^{2} \tag{16}$$

where N is the total number of the atoms considered; j denotes the atom next to atom i, α and R_{ref} are pre-calculated constants given in original paper for each type of atomic pair.

$$I = 100\left[1-\left(\frac{V}{V_K}\right)\right] \text{ where } V = \frac{100}{\bar{N}}\sqrt{\frac{\sum_i (N_{i,j}-\bar{N})^2}{n}}\ ;\ N_{i,j} = \frac{a}{R_{i,j}} - b \tag{17}$$

where i is the cycles all of the bonds in the ring; j denotes the atom next to atom i; n is the total number of the bonds considered; N denotes Gordy bond order; $\bar{N}$ is the average value of N values; $R_{i,j}$ is bond length; a and b are predefined parameters, respectively for each type of bonds; V_K is the pre-determined reference V.

$$\mathrm{PLR}(A,B) = \frac{\chi_{1,4}+\chi_{2,5}+\chi_{3,6}}{3} \tag{18}$$

Fig. 5 contains the information of ring 1, ring 2, ring 3 and ring 4.12N bearing ring is consider as ring 1, 28F bearing ring is referred as ring 3 and 27F bearing ring is taken as ring 4. Table-10 shows the aromaticity values for PDI, FLU, HOMA, BIRD and PLR. A higher aromatic nature is indicated by a low FLU number. The ring A is more aromatic in this instance than ring B. When HOMA equals 1, a ring is considered totally aromatic since the length of each bond is equal to the ideal value R_{Ref}. It is evident from Table-10 that ring C > ring B > ring A is the order of PDI aromaticity. The trend in FLU aromaticity is consistent: for example, ring C > ring B > ring A. The hierarchy for HOMA aromaticity is ring C > ring A > ring B, whereas the hierarchy of BIRD aromaticity is identified as ring C > ring A > ring B. The pattern of PLR parallels that of PDI and FLU.

Non-covalent interaction: Reduced density gradient (RDG), another name for non-covalent interaction, is a powerful method for comprehending non-covalent interactions inside molecules. The definition of RDG (eqn. 19) is:

$$\mathrm{RDG}_{(r)} = \frac{1}{2(3\pi^2)^{1/3}}\frac{|\Delta\rho(r)|}{\rho(r)^{4/3}} \tag{19}$$

TABLE-9
FUKUI FUNCTION VALUES OF VERICIGUAT MOLECULE

S. No.	MPA (a.u.)			NPA (a.u.)			$\Delta f(r)$
	fk^+	fk^-	$f^0(r)$	fk^+	fk^-	$f^0(r)$	
1 C	0.553	0.501	0.532	0.570	0.526	0.543	0.044
2 C	-0.306	-0.298	-0.306	-0.367	-0.278	-0.344	-0.089
3 N	-0.303	-0.381	-0.331	-0.492	-0.576	-0.528	0.084
4 C	0.058	-0.057	0.023	-0.053	-0.212	-0.088	0.159
5 C	0.055	-0.042	0.024	0.119	-0.047	0.088	0.166
6 C	0.184	0.151	0.162	0.211	0.180	0.174	0.031
7 N	-0.293	-0.341	-0.333	0.181	0.194	0.164	-0.013
8 N	-0.188	-0.302	-0.215	-0.455	-0.621	-0.485	0.166
9 C	0.193	0.132	0.160	0.315	0.129	0.228	0.186
10 C	0.001	0.025	0.010	-0.182	-0.190	-0.202	0.008
11 C	0.349	0.250	0.316	0.696	0.673	0.689	0.023
12 N	-0.414	-0.421	-0.429	-0.657	-0.714	-0.675	0.057
13 C	0.455	0.402	0.427	0.486	0.547	0.515	-0.061
14 C	0.060	-0.054	-0.007	0.046	-0.234	-0.149	0.28
15 N	-0.341	-0.376	-0.369	-0.663	-0.726	-0.710	0.063
16 C	0.412	0.364	0.386	0.550	0.604	0.598	-0.054
17 N	-0.427	-0.493	-0.471	-0.665	-0.794	-0.744	0.129
18 N	-0.441	-0.495	-0.477	-0.681	-0.775	-0.746	0.094
19 N	-0.471	-0.483	-0.490	-0.523	-0.473	-0.502	-0.05
20 C	0.532	0.507	0.519	0.839	0.816	0.831	0.023
21 C	-0.199	-0.186	-0.191	0.016	0.060	0.049	-0.044
22 C	-0.043	-0.040	-0.043	-0.174	-0.150	-0.171	-0.024
23 C	0.266	0.251	0.257	0.289	0.253	0.265	0.036
24 C	-0.085	-0.101	-0.094	-0.177	-0.210	-0.188	0.033
25 C	-0.097	-0.123	-0.110	-0.251	-0.260	-0.251	0.009
26 C	-0.070	-0.097	-0.083	-0.066	-0.132	-0.104	0.066
27 F	-0.225	-0.246	-0.237	-0.177	-0.197	-0.188	0.02
28 F	-0.200	-0.272	-0.236	-0.164	-0.234	-0.198	0.07
29 O	-0.384	-0.430	-0.415	-0.545	-0.591	-0.574	0.046
30 O	-0.338	-0.359	-0.352	-0.365	-0.410	-0.395	0.045
31 C	-0.118	-0.106	-0.111	-0.106	-0.054	-0.076	-0.052
32 H	0.139	0.075	0.118	0.175	0.155	0.167	0.02
33 H	0.161	0.065	0.124	0.148	0.099	0.123	0.049
34 H	0.167	0.124	0.146	0.114	0.071	0.097	0.043
35 H	0.180	0.111	0.153	0.179	0.105	0.151	0.074
36 H	0.244	0.205	0.217	0.380	0.351	0.359	0.029
37 H	0.255	0.216	0.235	0.358	0.348	0.356	0.01
38 H	0.239	0.194	0.216	0.324	0.292	0.311	0.032
39 H	0.256	0.208	0.226	0.385	0.346	0.362	0.039
40 H	0.276	0.224	0.244	0.347	0.294	0.316	0.053
41 H	0.115	0.127	0.123	0.174	0.181	0.180	-0.007
42 H	0.112	0.080	0.098	0.155	0.137	0.146	0.018
43 H	0.131	0.083	0.108	0.185	0.147	0.167	0.038
44 H	0.123	0.074	0.101	0.149	0.120	0.137	0.029
45 H	0.148	0.106	0.124	0.135	0.086	0.107	0.049
46 H	0.143	0.115	0.127	0.119	0.082	0.097	0.037
47 H	0.139	0.113	0.123	0.115	0.082	0.047	0.033

TABLE-10
VARIOUS AROMATICITY VALUES DETERMINED FOR VERICIGUAT MOLECULE

Rings	PDI	FLU	HOMA	BIRD	PLR
Ring A	0.0657	0.0116	0.9692	89.8248	0.3384
Ring B	0.0790	0.0112	0.9419	87.1723	0.4478
Ring C	0.0963	0.0024	0.9913	96.8735	0.5776

when sign (λ_2)ρ (a.u.) is plotted against RDG, some spikes are developed. According to the sign (λ_2) and the ρ values, the following regions are defined well. For example, strong attraction: halogen bond and hydrogen bond ($\rho > 0$ and $\lambda < 0$); van der Waals interaction: ($\rho \approx 0$ and $\lambda \approx 0$); and strong repulsion: steric effect in the ring and gage ($\rho > 0$ and $\lambda > 0$).

The non-covalent interaction (NCI) analysis of the molecule vericiguat was carried out using the Multiwfn 3.8 software and the result was viewed by VMD 1.9.4 tool and the corresponding visualisations are shown in Fig. 9. The results clearly indicate that vericiguat exhibits steric effects, van der Waals interactions and hydrogen bonding. Approximately -0.020 and +0.010 a.u. are the spikes that correlate to van der Waals forces of attraction. Steric effects inside the aromatic ring system are indicated by the spike about +0.020 a.u.

The resulting iso-surface (Fig. 9b) further supports the analysis. In the plot, brownish-green regions represent van der Waals interactions, red regions located at the center of the aromatic rings correspond to steric interactions and blue regions indicate the presence of hydrogen bonds. Thus, the NCI analysis of vericiguat reveals distinct non-covalent features: a spike in the negative region (-0.020 a.u.) confirms van der Waals interactions, the spike near +0.020 a.u. arises from steric effects and the spike around -0.020 a.u. is attributed to hydrogen bonding.

Shaded surface map with projection of LOL: According to Schmider & Becke [46], the localised orbital locator (LOL) is a crucial tool for locating high localisation regions such as ELF.

$$\mathrm{LOL}(r) = \frac{\tau(r)}{1+\tau(r)} \qquad \text{where, } (r) = \frac{D_0(r)}{\frac{1}{2}\sum_i \eta_{i|\nabla\phi_i|^2}} \qquad (20)$$

where $D_0(r)$ relates to closed-shell and spin-polarized systems, which are characterized in a manner analogous to ELF, LOL, and ELF, exhibiting a comparable relationship.

The shaded surface map for the analysed molecule depict the ester group, amino-group substituted pyrimidine moiety, pyrazolo-pyridine moiety and fluoro-phenyl group side views, respectively, thus clearly indicates the presence of LOL in the vicinity of the aromatic rings within the molecule (Fig. 10). The hydrogen atoms possess a significant quantity of electrons. Blue circles denote a segment of the molecule that has experienced electron loss and several aromatic carbon atoms have also experienced electron loss. Whereas all carbon and nitrogen atoms within the ring structure display an electron-deficient nature.

SAR with molecular docking: Human soluble guanylate cyclase (sGC) is an enzyme present inside the cells of blood vessels, especially in the heart, brain and lungs. Primarily, sGC is responsible for the relaxation of the blood vessels surrounding the heart. Nitric oxide (NO) is produced naturally by the body and is often released by the inner lining of blood vessels, the endothelium [47]. When NO is present inside the blood vessel, it binds to the heme group of the sGC protein enzyme [48]. After binding with NO, sGC becomes activated and converts guanosine triphosphate (GTP) into a secondary messenger nucleotide called cyclic guanosine monophosphate (*c*GMP) [49] and plays a crucial role in various cellular signaling pathways, including vasodilation, vascular smooth muscle motility, intestinal fluid and electrolyte homeostasis and retinal phototransduction [50,51]. In case of blood vessels surrounding the heart, *c*GMP signals the muscle cells in blood vessels to relax. This causes vasodilation, allowing the blood vessels to open up, which improves blood flow and leads to lower blood pressure.

However, in case of vericiguat, it works by binding directly to the sGC enzyme and becomes activated with or without the presence of NO. This further leads to the production of *c*GMP, which causes the relaxation of blood vessels [52]. Since it bypasses the NO mechanism, it works more efficiently, improving heart function in patients with heart failure and reducing

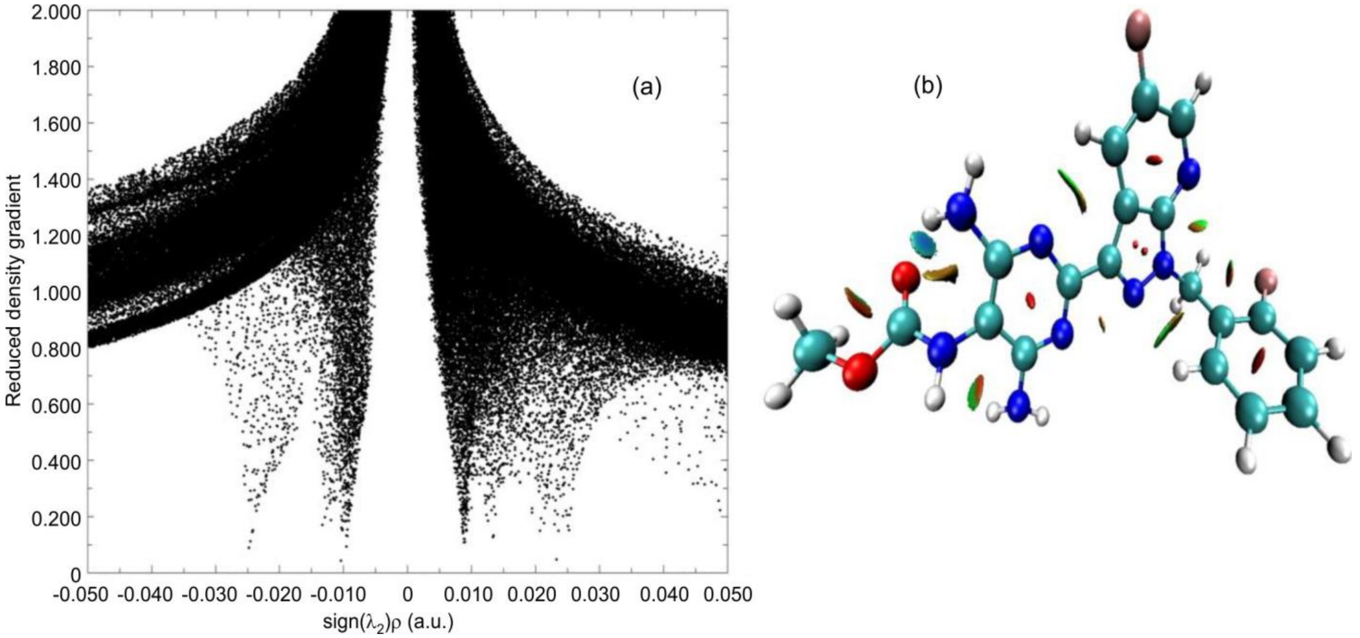

Fig. 9. (a) Non-covalent interaction and (b) iso-surface of vericiguat molecule

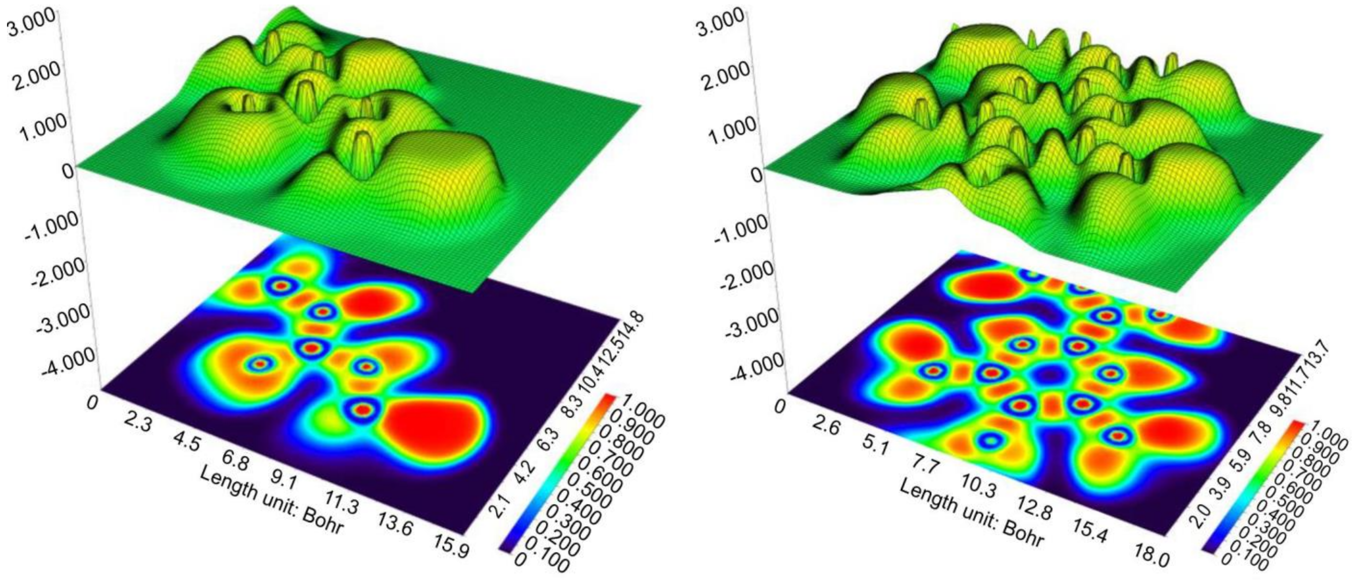

(a) Ester group side view

(b) Amino-group substituted pyrimidine moiety side view

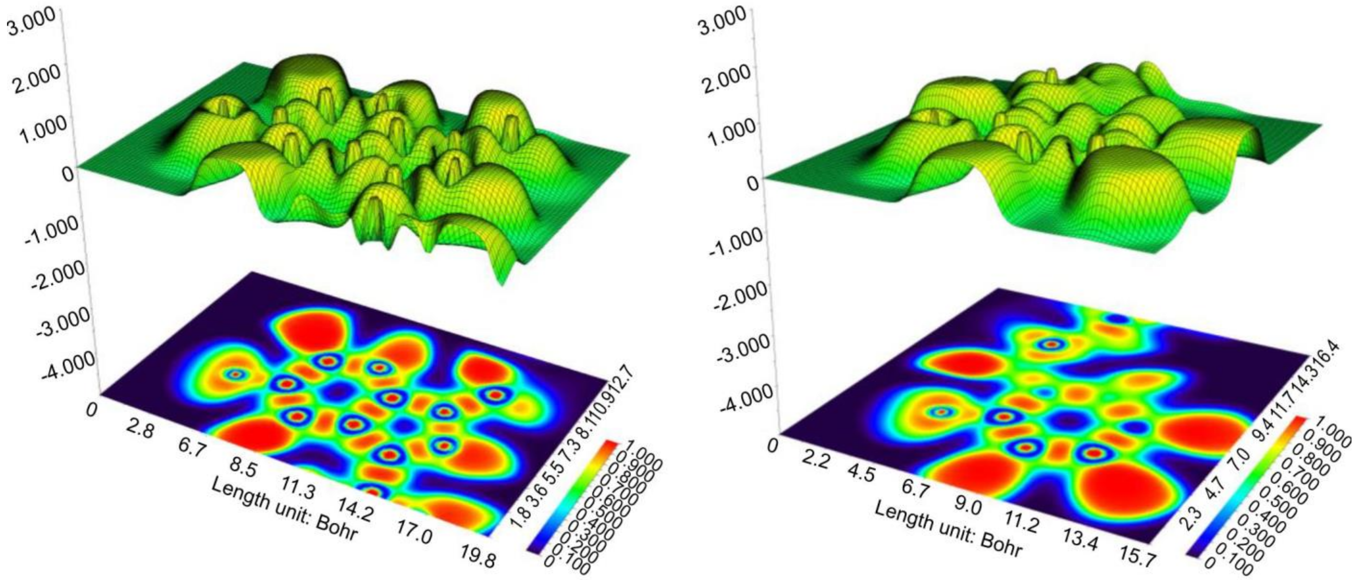

(c) Pyrazolo-pyridine moiety side view

(d) Fluoro-phenyl group side view

Fig. 10. Shaded surface map with projection of LOL for vericiguat

fatality rates. Based on the binding principle, vericiguat can be further modified for enhanced activity, which might yield a better inhibitor. Therefore, we designed fourteen different molecules by altering the position or changing the functional group Fig. 11.

Similar work was conducted by Acharya *et al*. [53], who improved binding activity by designing the structure of ACE inhibitors that led to more enhanced inhibition. Mobeen *et al*. [54], also worked on designing more potent DPP-4 inhibitors. Building on these ideas, our focus is to evaluate whether newly designed molecules promote stronger binding activity with the target protein, sGC (PDB ID: 6JT2) [19,20]. Such developments could contribute to reducing heart failure cases and fatality rates. To investigate this, a systematic molecular docking approach is employed to identify the interactions between the designed molecules and the target protein [21]. Docking simulations were performed using the Maestro docking tool [23]. In this context, we implemented the Induced Fit Docking (IFD) method, allowing adjustments in both protein side chains and ligand structures to achieve optimal binding interactions. Twenty docking poses were generated as a result of this approach [55,56]. Docking scores served as key indicators of binding strength, while further analysis of protein–ligand interactions provided insights into binding site residues and the stability of the complexes [57]. The docking scores and the interacting residues with 6JT2 are shown in Table-11. For a more comprehensive visualisation, the 3D interaction diagrams of the top-performing compounds V1Br, V1F and V1NO_2 are illustrated in Fig. 12.

This analysis focuses on identifying the binding strength of the parent molecule vericiguat and the newly designed molecules. All molecules resulted in negative docking scores ranging

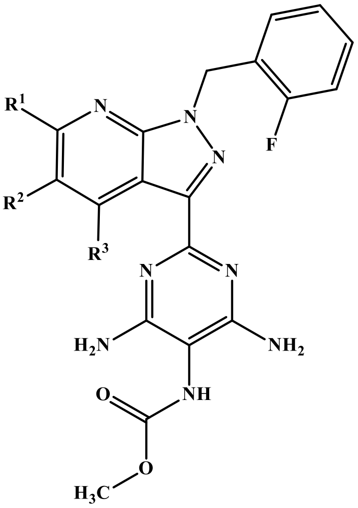

Molecules	R^1	R^2	R^3
V1F	F	H	H
V2F	H	F	H
V3F	H	H	F
V1Cl	Cl	H	H
V2Cl	H	Cl	H
V3Cl	H	H	Cl
V1Br	Br	H	H
V2Br	H	Br	H
V3Br	H	H	Br
V1COOH	COOH	H	H
V2COOH	H	COOH	H
V3COOH	H	H	COOH
V1NO_2	NO_2	H	H
V2NO_2	H	NO_2	H
V3NO_2	H	H	NO_2

Fig. 11. Different modification representation of vericiguat

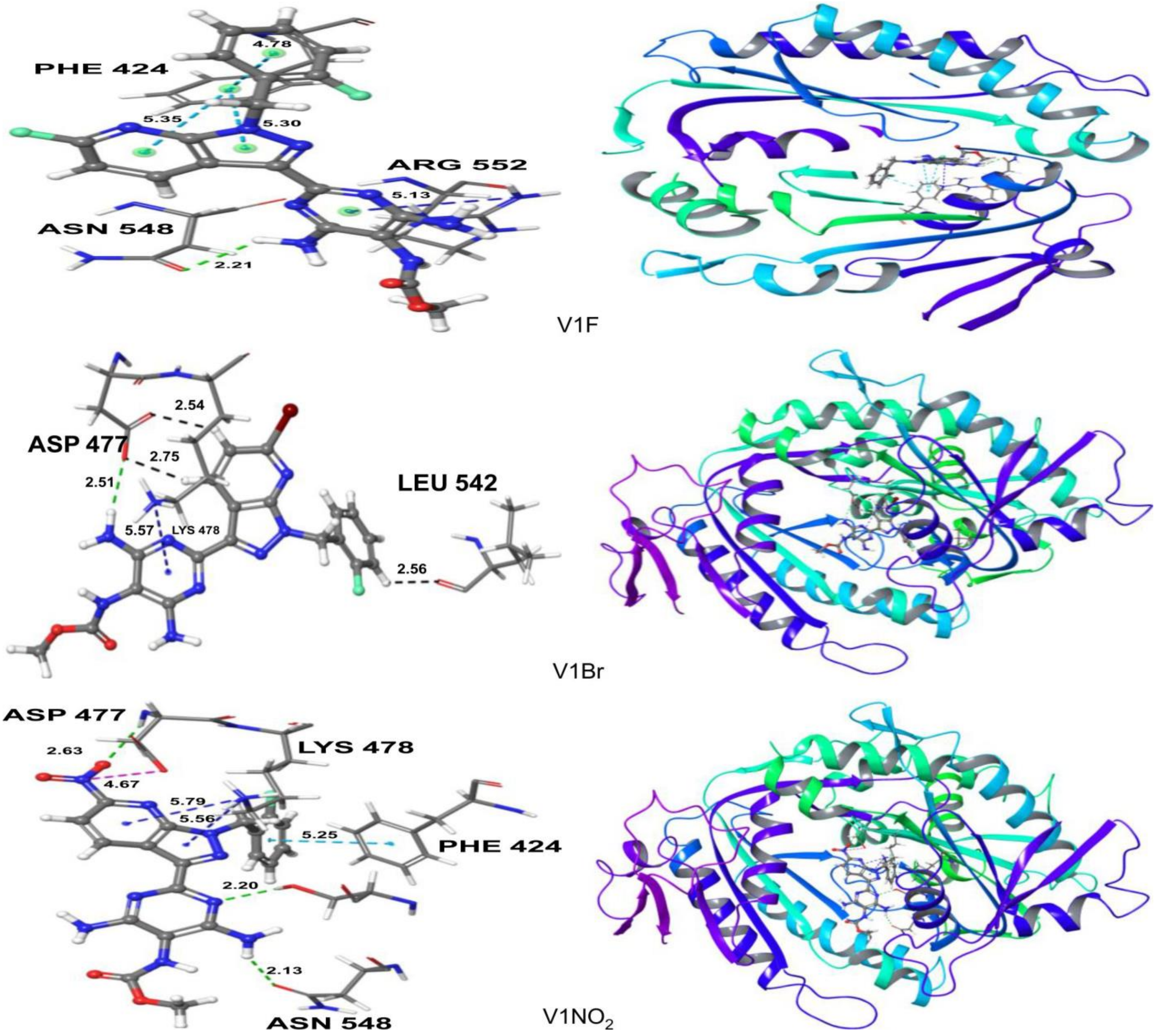

Fig. 12. Docking images of V1F, V1Br, V1NO_2 with the protein 6JT2

TABLE-11
MOLECULAR DOCKING RESULTS OF VERICIGUAT WITH HUMAN SOLUBLE GUANYLATE CYCLASE (PDB ID: 6JT2)

Molecules	Docking score (kcal/mol)	Interacting residues	Interaction distance (Å)
Parent	-9.713	LEU 542 (Aromatic-hydrogen-bonding)	2.73
		PHE 424 (Pi-pi stacking)	5.25
		ARG 552 (Pi-cation)	5.66
V1F	-10.705	PHE 424 (Pi-pi stacking)	4.78
		PHE 424 (Pi-pi stacking)	5.39
		PHE 424 (Pi-pi stacking)	5.35
		ARG 552 (Pi-cation)	5.13
		ASN548 (Halogen-bonding)	2.24
V3F	-9.894	LEU 542 (Aromatic-hydrogen-bonding)	2.49
		PHE 424 (Pi-pi stacking)	5.46
		ARG 593 (Pi-cation)	6.40
V1Cl	-9.445	GLU 473 (Aromatic-hydrogen-bonding)	2.91
		PHE 543 (Pi-pi stacking)	5.25
		PHE 424 (Pi-pi stacking)	5.18
		ARG 552 (Pi-cation)	5.65
V2Cl	-10.365	LEU 542 (Aromatic-hydrogen-bonding)	2.74
		GLY 544 (Halogen-bonding)	2.55
		ASN548 (Aromatic-hydrogen-bonding)	2.51
		ARG 552 (Hydrogen-bonding)	2.47
V3Cl	-10.520	PHE 424 (Pi-pi stacking)	5.26
		LEU 542 (Aromatic-hydrogen-bonding)	2.29
		ASN548 (Hydrogen-bonding)	1.83
		ASN548 (Hydrogen-bonding)	1.99
V1Br	-10.785	LEU 542 (Aromatic-hydrogen-bonding)	2.56
		LYS 478 (Pi-cation)	5.57
		Asp 477 (Hydrogen-bonding)	2.51
		ASP 477 (Aromatic-hydrogen-bonding)	2.76
		ASP 477 (Aromatic-hydrogen-bonding)	2.54
V2Br	-10.408	GLY 544 (Halogen-bonding)	2.54
		ASN548 (Hydrogen-bonding)	2.18
		ARG 552 (Pi-cation)	5.06
V3Br	-10.380	PHE 424 (Pi-pi stacking)	5.33
		PHE 424 (Pi-pi stacking)	5.32
		PHE 424 (Pi-pi stacking)	5.48
		LYS 478 (Pi-cation)	6.51
		SER 551 (Hydrogen-bonding)	2.39
		ASN548 (Halogen-bonding)	3.38
		ARG 552 (Hydrogen-bonding)	2.48
V1COOH	-9.547	GLU 473 (Aromatic-hydrogen-bonding)	2.21
		PHE 543 (Pi-pi stacking)	5.40
		PHE 424 (Pi-pi stacking)	5.16
		PHE 424 (Pi-pi stacking)	4.76
V2COOH	-8.539	ASP 477 (Aromatic-hydrogen-bonding)	2.27
		ASP 477 (Hydrogen-bonding)	1.63
		LYS 478 (Pi-cation)	5.60
		LYS 478 (Pi-cation)	6.04
V3COOH	-9.904	LYS 478 (Pi-cation)	6.45
		LYS 478 (Pi-cation)	6.19
		ILE 528 (Hydrogen-bonding)	2.35
		ASN548 (Pi-cation)	3.01
		ARG 552 (Hydrogen-bonding)	1.78
V1NO$_2$	-10.444	ASP 477 (Hydrogen-bonding)	2.63
		ASP 477 (Salt-bridge)	4.67
		LYS 478 (Pi-cation)	5.79
		LYS 478 (Pi-cation)	5.56
		PHE 424 (Pi-pi stacking)	5.25
		SER 551 (Hydrogen-bonding)	2.20
		ASN548 (Hydrogen-bonding)	2.13

V2NO$_2$	-8.552	ASP 477 (Aromatic-hydrogen-bonding)	2.57
		ASP 477 (Aromatic-hydrogen-bonding)	3.89
		VAL 547 (Hydrogen-bonding)	2.46
		VAL 547 (Hydrogen-bonding)	2.54
		ASN548 (Hydrogen-bonding)	2.01
		ASP 530 (Hydrogen-bonding)	2.46
		PHE 484 (Pi-pi stacking)	5.00
		GLH 608 (Aromatic-hydrogen-bonding)	2.63
V3NO$_2$	-9.958	ARG 552 (Hydrogen-bonding)	2.06
		ARG 552 (Hydrogen-bonding)	2.20
		ARG 552 (Salt-bridge)	4.61
		ARG 552 (Pi-cation)	3.50
		GLY 489 (Hydrogen-bonding)	2.54

from -10.785 to -8.539 kcal/mol, which indicates stronger binding interactions with the target protein. Among the designed molecules, 10 out of 14 showed better binding strength than the parent molecule vericiguat, which recorded a docking score of -9.719 kcal/mol. Vericiguat interacts with residue LEU 542 through aromatic hydrogen bonding at a distance of 2.73 Å, indicating a stronger interaction due to the shorter distance. Additional interactions include residue PHE 424 *via* π-π stacking at 5.25 Å and ARG 552 *via* π-cation bonding at 5.66 Å. V1Br achieved the best docking score of -10.785 kcal/mol, indicating much stronger binding strength along with a greater number of interacting residues compared with the parent molecule. One key interaction is with residue ASP 477, which forms dual aromatic hydrogen bonds at distances of 2.54 Å and 2.77 Å. Additional interactions include LEU 542 and LYS 478 through aromatic hydrogen bonding and π-cation bonding, with interaction distances of 2.56 Å and 5.57 Å, respectively. V1Br therefore exhibited four strong interactions with protein residues and also V1NO$_2$ also showed promising results, with a docking score of -10.444 kcal/mol. ASP 477 interacts at two sites *via* hydrogen bonding and a salt bridge at distances of 2.63 Å and 4.67 Å, whereas LYS 478 interacts twice *via* π-cation bonding, with distances of 5.56 Å and 5.79 Å.

For V1F, changing the position of the anchoring fluorine yielded excellent improvement in binding strength, with a docking score of -10.705 kcal/mol. This enhancement is due to strong halogen bonding with residue ASN 548 at a distance of 2.24 Å. Furthermore, the core residue PHE 424 interacts through three different π-π stacking interactions at distances of 4.78 Å, 5.39 Å and 5.35 Å, while ARG 552 interacts *via* π-cation bonding at 5.13 Å. V1NO$_2$ also shows three more key interactions, involving residues PHE 424, SER 551 and ASN 548.

Among these, SER 551 and ASN 548 interact *via* strong hydrogen bonding at distances of 2.20 Å and 2.13 Å, while PHE 424 interacts through π-π stacking. Seven other designed molecules also outperformed the parent molecule due to their interactions with key residues such as ARG 552, ASP 477 and LYS 478 *via* multiple binding modes, in some cases forming stronger interactions than those observed for the parent compound. While analyzing the interacting residues across all the molecules, repeated ligand contact points were revealed. ARG 552 frequently appears across multiple molecules (V1F, V1Cl, V2Cl, V2Br, V3Br, V3COOH, V3NO$_2$), involved in varied interactions such as π-cation, salt bridge and hydrogen bonding. This residue likely plays a critical role in ligand anchoring. Similarly, PHE 424 and ASN 548 also show recurring involvement, suggesting that maintaining interactions with these residues may be key for future ligand optimisation. V1Br showed the importance of multiple strong interactions with shorter distances, leading to stronger bonding with the highest docking score, aligning with the literature that correlates shorter hydrogen bond distances with increased binding affinity [58]. These findings highlight the importance of positional changes and structural design in achieving better binding compared to the parent molecule. Furthermore, the results not only identified, which designed molecules outperformed the parent molecule but also highlighted key binding spots that could be used for the rational design of next-generation inhibitors.

Conclusion

From the geometry and vibrational analyses, the bond lengths, bond angles, dihedral angles and IR values of the vericiguat molecule. These values were compared with previous literature reports and verified whether vericiguat possesses similar chemical properties; it came up with good agreement. Mulliken charge analysis provided the atomic charge distribution for each atom. The calculated quantum chemical parameters offered deeper insight into the electronic structure of vericiguat and these values were subsequently used to design docking molecules in the later stage of the study. The electrostatic potential map allowed to visualize the electronic environment of vericiguat, while the natural bond orbital (NBO) analysis revealed the pathways of electron delocalisation, particularly the tendency of electron density to migrate toward the fluorine atom. These finding might help to explain variations in docking scores when atomic positions are altered in future studies as well. The hole-electron interaction analysis further clarified the nature of electronic excitations within the molecule. The UV-Vis spectral data provided information on excitation energies and absorption peaks, along with the contributions of various HOMO–LUMO orbitals. Fukui function analysis identified the most probable sites for electrophilic, nucleophilic and radical attacks across the molecule. Aromaticity analysis highlighted which ring systems possess greater aromatic character in vericiguat. The noncovalent interaction (NCI) analysis indicated the presence of weak intermolecular interactions within the molecule. In addition, the shaded surface map combined with localised orbital locator (LOL) projecttions revealed potential regions of electron depletion, which may play a role in future reactivity and molecular design. By integrating all these results, we designed 14 novel derivatives from the parent molecule. Among them, the derivative V1F demonstrated more favourable properties than the parent compound and could potentially serve as a better candidate for heart failure treatment. However, further experimental validation is required to confirm the therapeutic promise of V1F as a more potent inhibitor compared to the parent molecule.

ACKNOWLEDGEMENTS

The authors thank the authorities of St. John's College and Dr. Vijay Solomon, Assistant Professor of Chemistry, Madras Christian College for supplying computers and software facilities.

CONFLICT OF INTEREST

The authors declare that there is no conflict of interests regarding the publication of this article.

DECLARATION OF AI-ASSISTED TECHNOLOGIES

The authors declare that no AI tools were used in the preparation or writing of this research/review article.

REFERENCES

1. P.W. Armstrong, B. Pieske, K.J. Anstrom, J. Ezekowitz, J. Butler, A.F. Hernandez, C.S.P. Lam, P. Ponikowski, A.A. Voors, S.E. McNulty, G. Jia, M.J. Patel, L. Roessig, J. Koglin and C.M. O'Connor, *N. Engl. J. Med.*, **382**, 1883 (2020); https://doi.org/10.1056/NEJMoa1915928
2. C. Kang and Y.N. Lamb, *Am. J. Cardiovasc. Drugs*, **22**, 451 (2022); https://doi.org/10.1007/s40256-022-00538-5
3. A.K. Siddiqi, S.J. Greene, M. Fudim, R.J. Mentz, J. Butler and M.S. Khan, *Expert Rev. Cardiovasc. Ther.*, **21**, 245 (2023); https://doi.org/10.1080/14779072.2023.2189101
4. A.J. Coats and H. Tolppanen, *Drugs*, **81**, 1599 (2021); https://doi.org/10.1007/s40265-021-01586-y
5. M. Senni, J. Lopez-Sendon, A. Cohen-Solal, P. Ponikowski, R. Nkulikiyinka, C. Freitas, V.M. Vlajnic, L. Roessig and B. Pieske, *ESC Heart Fail.*, **9**, 3791 (2022); https://doi.org/10.1002/ehf2.14050
6. A. Olivella, L. Almenar-Bonet, P. Moliner, E. Coloma, A. Martínez-Rubio, M. Paz Bermejo, R. Boixeda, G. Cediel, A.B. Méndez Fernández and L. Facila Rubio, *ESC Heart Fail.*, **11**, 628 (2024); https://doi.org/10.1002/ehf2.14647
7. C.M. Lombardi, G. Cimino, M. Pagnesi, A. Dell'Aquila, D. Tomasoni, A. Ravera, R. Inciardi, V. Carubelli, E. Vizzardi, S. Nodari, M. Emdin and A. Aimo, *Curr. Cardiol. Rep.*, **23**, 144 (2021); https://doi.org/10.1007/s11886-021-01580-6
8. B.A. Tran, E.S. Serag-Bolos, J. Fernandez and A.C. Miranda, *J. Pharm. Pract.*, **36**, 905 (2023); https://doi.org/10.1177/08971900221087096
9. C. Chen, J. Lv and C. Liu, *Front. Endocrinol.*, **15**, 1335531 (2024); https://doi.org/10.3389/fendo.2024.1335531
10. C. Elıjah, *J. Turkish Chem. Soc.*, **7**, 77 (2020); https://doi.org/10.18596/jotcsa.527827
11. B.K. Shukla and U. Yadava, *Mater. Today Proc.*, **49**, 3056 (2022); https://doi.org/10.1016/j.matpr.2020.10.903
12. X. Zhang and Z. Geng, *RSC Advances*, **6**, 62099 (2016); https://doi.org/10.1039/C6RA07780C
13. K.B. Rai, R.R. Ghimire, C. Dhakal, K. Pudasainee and B. Siwakoti, *J. Nepal Chemical Soc.*, **44**, 1 (2024); https://doi.org/10.3126/jncs.v44i1.62675
14. R.G. Parr, Density Functional Theory of Atoms and Molecules, In: Horizons of Quantum Chemistry: Proceedings of the Third International Congress of Quantum Chemistry Held at Kyoto, Japan, October 29-November 3, 1979. 1989. Springer.
15. M.J. Frisch, G.W. Trucks, H.B. Schlegel, G.E. Scuseria, M.A. Robb, J.R. Cheeseman, G. Scalmani, V. Barone, G.A. Petersson, H. Nakatsuji, X. Li, M. Caricato, A.V. Marenich, J. Bloino, B.G. Janesko, R. Gomperts, B. Mennucci, H.P. Hratchian, J.V. Ortiz, A.F. Izmaylov, J.L. Sonnenberg, D. Williams-Young, F. Ding, B. Peng, F. Lipparini, F. Egidi, J. Gao, J. Goings, A. Petrone, T. Henderson, D. Ranasinghe, V.G. Zakrzewski, N. Rega, G. Zheng, W. Liang, M. Hada, M. Ehara, K. Toyota, R. Fukuda, J. Hasegawa, M. Ishida, T. Nakajima, Y. Honda, O. Kitao, H. Nakai, T. Vreven, K. Throssell, J.A. Montgomery Jr., J.E. Peralta, F. Ogliaro, M.J. Bearpark, J.J. Heyd, E.N. Brothers, K.N. Kudin, V.N. Staroverov, T.A. Keith, R. Kobayashi, J. Normand, K. Raghavachari, A.P. Rendell, J.C. Burant, S.S. Iyengar, J. Tomasi, M. Cossi, J.M. Millam, M. Klene, C. Adamo, R. Cammi, J.W. Ochterski, K. Morokuma, R.L. Martin, O. Farkas, J.B. Foresman and D.J. Fox, Gaussian 16, Revision B.01. Wallingford, CT, USA: Gaussian, Inc. (2016).
16. R. Dennington, T. Keith and J. Millam, GaussView, Version 5.0. Wallingford, CT, USA: Gaussian, Inc. (2009).
17. N.M. O'boyle, A.L. Tenderholt and K.M. Langner, *J. Comput. Chem.*, **29**, 839 (2008); https://doi.org/10.1002/jcc.20823
18. W. Humphrey, A. Dalke and K. Schulten, *J. Mol. Graph.*, **14**, 33 (1996); https://doi.org/10.1016/0263-7855(96)00018-5
19. T. Lu and F. Chen, *J. Comput. Chem.*, **33**, 580 (2012); https://doi.org/10.1002/jcc.22885
20. Y. Kang, R. Liu, J.-X. Wu and L. Chen, *Nature*, **574**, 206 (2019); https://doi.org/10.1038/s41586-019-1584-6
21. G. Wu, I. Sharina and E. Martin, *Front. Mol. Biosci.*, **9**, 1007768 (2022); https://doi.org/10.3389/fmolb.2022.1007768
22. G. Madhavi Sastry, M. Adzhigirey, T. Day, R. Annabhimoju and W. Sherman, *J. Comput. Aided Mol. Des.*, **27**, 221 (2013); https://doi.org/10.1007/s10822-013-9644-8.
23. A.M. Omar, A.S. Aljahdali, M.K. Safo, G.A. Mohamed and S.R.M. Ibrahim, *Molecules*, **28**, 44 (2022); https://doi.org/10.3390/molecules28010044
24. X.L. Fan, X.-Q. Wang, J.-T. Wang and H.-D. Li, *Phys. Lett. A*, **378**, 1379 (2014); https://doi.org/10.1016/j.physleta.2014.03.035
25. M.R. Silva, A.M. Beja, J.A. Paixão, L.L.G. Justino and A.J.F.N. Sobral, *J. Mol. Struct.*, **785**, 32 (2006); https://doi.org/10.1016/j.molstruc.2005.09.037
26. J.L. Gázquez, *J. Mex. Chem. Soc.*, **52**, 3 (2008).
27. S.B. Liu, *Wuli Huaxue Xuebao*, **25**, 590 (2009); https://doi.org/10.3866/PKU.WHXB20090332
28. P. Geerlings, F. De Proft and W. Langenaeker, *Chem. Rev.*, **103**, 1793 (2003); https://doi.org/10.1021/cr990029p
29. H. Chermette, *J. Comput. Chem.*, **20**, 129 (1999); https://doi.org/10.1002/(SICI)1096-987X(19990115)20:1<129::AID-JCC13>3.0.CO; 2-A
30. L.H. Mendoza-Huizar, *J. Chem.*, **2015**, 751527 (2015); https://doi.org/10.1155/2015/751527
31. P.K. Chattaraj, U. Sarkar and D.R. Roy, *Chem. Rev.*, **106**, 2065 (2006); https://doi.org/10.1021/cr100149p
32. J.I. Martínez-Araya, G. Salgado-Moran and D. Glossman-Mitnik, *J. Phys. Chem. B*, **117**, 6339 (2013); https://doi.org/10.1021/jp400241q
33. J.L. Gázquez, A. Cedillo and A. Vela, *J. Phys. Chem. A*, **111**, 1966 (2007); https://doi.org/10.1021/jp065459f
34. L.R. Domingo, M. Ríos-Gutiérrez and P. Pérez, *Molecules*, **21**, 748 (2016); https://doi.org/10.3390/molecules21060748
35. S. Xavier, S. Periandy and S. Ramalingam, *Spectrochim. Acta A Mol. Biomol. Spectrosc.*, **137**, 306 (2015); https://doi.org/10.1016/j.saa.2014.08.039
36. Z. Demircioğlu, Ç.A. Kaştaş and O. Büyükgüngör, *J. Mol. Struct.*, **1091**, 183 (2015); https://doi.org/10.1016/j.molstruc.2015.02.076
37. H. Wang, S. Chen, D. Yong, X. Zhang, S. Li, W. Shao, X. Sun, B. Pan and Y. Xie, *J. Am. Chem. Soc.*, **139**, 4737 (2017); https://doi.org/10.1021/jacs.6b12273

38. Z. Liu, T. Lu and Q. Chen, *Carbon*, **165**, 461 (2020); https://doi.org/10.1016/j.carbon.2020.05.023
39. M. Al-Zharani, M.S. Al-Eissa, H.A. Rudayni, D. Ali, S. Alkahtani, R. Surendrakumar and A. Idhayadhulla, *J. King Saud Univ. Sci.*, **34**, 101767 (2022); https://doi.org/10.1016/j.jksus.2021.101767
40. W. Coblentz, Investigations of Infrared Spectra, Carnegie Institution of Washington, DC (1905).
41. J. Poater, M. Duran, M. Solà and B. Silvi, *Chem. Rev.*, **105**, 3911 (2005); https://doi.org/10.1021/cr030085x
42. C. Bird, *Tetrahedron*, **41**, 1409 (1985); https://doi.org/10.1016/S0040-4020(01)96543-3
43. E. Matito, M. Duran and M. Solà, *J. Chem. Phys*., **122**, 014109 (2005); https://doi.org/10.1021/acs.joc.3c01539
44. T.M. Krygowski, *J. Chem. Inf. Comput. Sci.*, **33**, 70 (1993); https://doi.org/10.1021/ci00011a011
45. N. Sablon, F. De Proft, M. Solà and P. Geerlings, *Phys. Chem. Chem. Phys.*, **14**, 3960 (2012); https://doi.org/10.1039/c2cp23372j
46. H. Schmider and A. Becke, *J. Mol. Struct. Theochem.*, **527**, 51 (2000); https://doi.org/10.1016/S0166-1280(00)00477-2
47. Y. Zhao, P.M. Vanhoutte and S.W. Leung, *J. Pharmacol. Sci.*, **129**, 83 (2015); https://doi.org/10.1016/j.jphs.2015.09.002
48. P.M. Schmidt, M. Schramm, H. Schröder, F. Wunder and J.-P. Stasch, *J. Biol. Chem.*, **279**, 3025 (2004); https://doi.org/10.1074/jbc.M310141200
49. J.W. Denninger and M.A. Marletta, *Biochim. Biophys. Acta Bioenerg.*, **1411**, 334 (1999); https://doi.org/10.1016/S0005-2728(99)00024-9
50. S.H. Francis, J.L. Busch and J.D. Corbin, *Pharmacol. Rev.*, **62**, 525 (2010); https://doi.org/10.1124/pr.110.002907
51. N.I. Bork and V.O. Nikolaev, *Int. J. Mol. Sci.*, **19**, 801 (2018); https://doi.org/10.3390/ijms19030801
52. M. Vohra, M. Amir, I. Osoro, A. Sharma and R. Kumar, *Glob. Health J.*, **7**, 123 (2023); https://doi.org/10.1016/j.glohj.2023.07.004
53. K.R. Acharya, E.D. Sturrock, J.F. Riordan and M.R.W. Ehlers, *Nat. Rev. Drug Discov.*, **2**, 891 (2003); https://doi.org/10.1038/nrd1227
54. B. Mobeen, M. Shah, H.M. Rehman, M.S. Jan and U. Rashid, *Eur. J. Med. Chem.*, **279**, 116834 (2024); https://doi.org/10.1016/j.ejmech.2024.116834
55. R. Lipin, A.K. Dhanabalan, K. Gunasekaran and R.V. Solomon, *SN Appl. Sci.*, **3**, 110 (2021); https://doi.org/10.1007/s42452-020-04051-9
56. J.A. Bell, Y. Cao, J.R. Gunn, T. Day, E. Gallicchio, Z. Zhou, R. Levy and R. Farid, *Int. Tables Crystallogr*., **F**, 534 (2012); https://doi.org/10.1107/97809553602060000864
57. R. Farid, T. Day, R.A. Friesner and R.A. Pearlstein, *Bioorg. Med. Chem.*, **14**, 3160 (2006); https://doi.org/10.1016/j.bmc.2005.12.032
58. W. Sherman, T. Day, M.P. Jacobson, R.A. Friesner and R. Farid, *J. Med. Chem.*, **49**, 534 (2006); https://doi.org/10.1021/jm050540c